Delft University of Technology

Phase Estimation for Distributed Scatterers in InSAR Stacks Using Integer Least Squares Estimation

Samiei-Esfahany, Sami; Martins, Joana Esteves; Van Leijen, Freek; Hanssen, Ramon F.

Phase Estimation for Distributed Scatterers in InSAR Stacks Using Integer Least Squares Estimation

Sami Samiei-Esfahany, Joana Esteves Martins, Freek van Leijen, and Ramon F. Hanssen, *Member, IEEE*

Abstract—In recent years, new algorithms have been proposed to retrieve maximum available information in synthetic aperture radar (SAR) interferometric stacks with focus on distributed scatterers. The key step in these algorithms is to optimally estimate single-master (SM) wrapped phases for each pixel from all possible interferometric combinations, preserving useful information and filtering noise. In this paper, we propose a new method for SM-phase estimation based on the integer least squares principle. We model the SM-phase estimation problem in a linear form by introducing additional integer ambiguities and use a bootstrap estimator for joint estimation of SM-phases and the integer unknowns. In addition, a full error propagation scheme is introduced in order to evaluate the precision of the final SM-phase estimates. The main advantages of the proposed method are the flexibility to be applied on any (connected) subset of interferograms and the quality description via the provision of a full covariance matrix of the estimates. Results from both synthetic experiments and a case study over the Torfajökull volcano in Iceland demonstrate that the proposed method can efficiently filter noise from wrapped multibaseline interferometric stacks, resulting in doubling the number of detected coherent pixels with respect to conventional persistent scatterer interferometry.

Index Terms—Distributed scatterers (DS), integer least squares (ILS), interferometric synthetic aperture radar (InSAR), phase linking, phase triangulation, radar interferometry.

I. INTRODUCTION

SINCE the late 1990s, different methodologies have been developed for processing interferometric synthetic aperture radar (InSAR) data stacks, with applications in detecting and measuring various ground deformation phenomena. A class of time-series InSAR techniques, called persistent scatterer interferometry (PSI), focuses on point targets with high phase stability (*persistent scatterers* or PS) in the entire data stack, which are minimally affected by temporal and geometrical decorrelation [1]–[6]. Some other methodologies extract information also from targets that are affected by decorrelation, called *distributed scatterers* (DS), which contain coherent information only in some interferometric pairs, usually with shorter temporal and spatial baselines. The first efforts to extract information from DS were developed using the idea of stacking and exploiting different subsets of interferograms [7]–[14],

followed by the concept of small-baseline subsets (SB) [15], [16]. In the latter, SB interferograms are selected to minimize the effect of decorrelation and are multilooked (i.e., averaged with neighboring pixels) to further reduce the decorrelation, and then, they are spatially unwrapped. After unwrapping, a single-master (SM) phase time-series (i.e., the phase differences with respect to one acquisition called the master) for each pixel is estimated from all of the unwrapped SB interferograms by least squares or singular value decomposition. Clearly, this final SM-phase estimation requires reliable phase unwrapping of every single SB interferogram prior to the estimation.

More recent multimaster (MM) approaches [17], [18] proposed to swap the sequence order, and they perform SM time-series estimation before unwrapping. In other words, in the first step, SM (wrapped) phase time-series are estimated from wrapped MM interferograms, followed by (spatial, temporal, or spatiotemporal) unwrapping of the estimated SM interferogram stack. From a physical point of view, the preunwrapping estimation of SM-phase filters out the decorrelation noise and estimates the (wrapped) phase time-series corresponding to the physical path differences between the targets and the sensor. In this way, the signal-to-noise ratio of the pixels is improved, yielding an improved unwrapping. The preunwrapping estimation of SM-phases is called *phase linking* in [17], as the estimated phases are results of linking (or joint processing) all available interferometric phases, or *phase triangulation* in SqueeSAR [18], as the estimation is done based on phase consistency or triangularity condition (cf., Section III). We will refer to "*SM-phase* estimation" in the remainder of this paper.

The current SM-phase estimation methods [17]–[21] are all based on nonlinear optimization. These methods solve the nonlinear problem either by iterative algorithms initialized by subjective choice of initial values or by eigendecomposition of full coherence/covariance matrix of a data stack. Some of these algorithms are very demanding (especially in large stacks) by requiring all of the interferometric phase combinations (or the full complex coherence matrix for every pixel). In addition to these algorithms, an alternative heuristic yet effective approach called *multilink InSAR* [22] has been introduced. This approach constructs versions of every SM interferogram using different interferometric paths, combining them to obtain an estimate for each SM interferogram. However, the selection of paths and interferograms is still subjective. Regarding the quality description of the estimated SM-phases, although [17] has introduced a generic presentation of highest achievable precision in the form of lower Cramér–Rao bound (CRB), there is no formal quality description in the form of a full covariance matrix of final phase estimates.
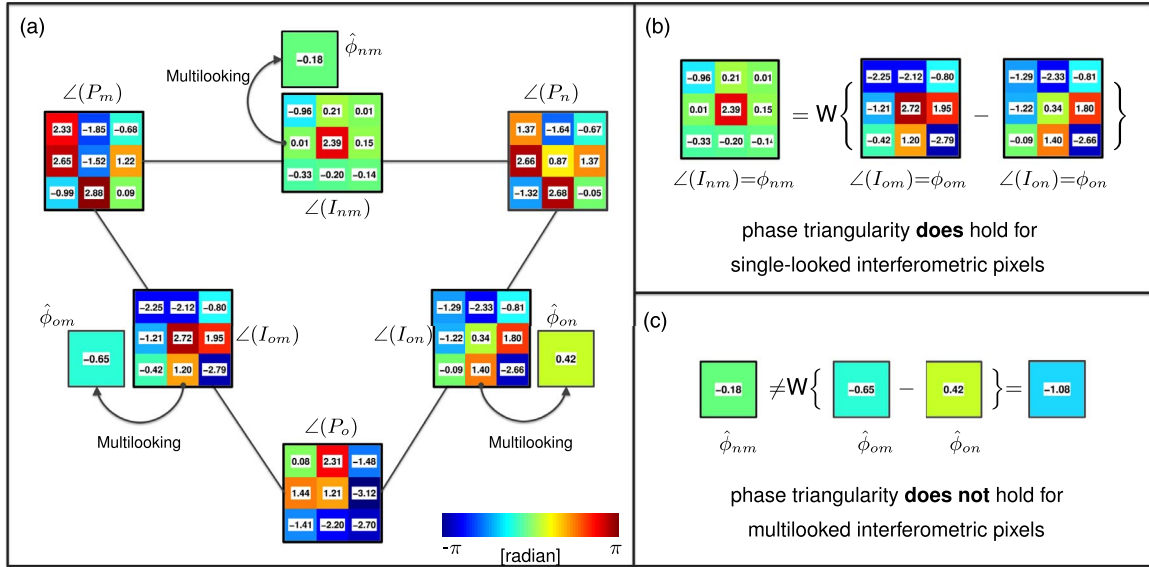
Fig. 1. Numerical demonstration of phase triangularity. (a) Three 3×3 phase interferograms $(\phi_{om}, \phi_{on}, \phi_{nm})$ constructed from the 3×3 SLC phases $(\angle(P_o), \angle(P_m), \angle(P_n))$ and the corresponding multilooked interferometric phases $(\hat{\phi}_{om}, \hat{\phi}_{on}, \hat{\phi}_{nm})$. (b) Demonstration of the phase triangularity condition for single-looked pixels. (c) Demonstration of the triangularity condition failing for multilooked pixels.

In this paper,[1] we present a new method for SM-phase estimation based on integer least squares (ILS) principle. ILS is a geodetic estimation method, originally designed for GPS applications [24]–[26], and later also applied to InSAR temporal phase unwrapping [3], [27]–[29]. We model the SM-phase estimation problem as a system of linear observation equations with some integer and real unknowns, and use ILS to estimate unknown parameters. The advantage is that ILS considers all of the mutual correlations between interferometric phases and allows formal error propagation from the observations to the final estimates. As a result, the full covariance matrix of the estimated phases is provided. Furthermore, the model can be applied to any subset of interferograms. This is beneficial especially for large stacks where the computation of all possible interferograms can be cumbersome.

This paper is organized as follows. We first describe the general concept of phase triangularity (Section II), followed by the proposed mathematical model (Section III). In Section IV, we introduce the ILS estimator and its application to SM-phase estimation. Practical considerations are given in Section V. Synthetic experiments and real data results are presented in Sections VI and VII, followed by the conclusion in Section VIII.

II. PHASE TRIANGULARITY

Assume that $\underline{P}_m$, $\underline{P}_n$, and $\underline{P}_o$ are three coregistered single-look complex (SLC) images (see Fig. 1 as a simplistic example) in the form of

$$\underline{P}_m = \underline{A}_m \exp(j\underline{\psi}_m) \tag{1}$$

where j is the imaginary unit and $\underline{A}_m \in \mathbb{R}^+$ and $\underline{\psi}_m \in [-\pi, \pi)$ represent the amplitude and phase of $\underline{P}_m$, respectively. Underlined letters (e.g., $\underline{I}$) denote stochastic variables/vectors. The single-look interferograms $\underline{I}_{om}$, $\underline{I}_{on}$, and $\underline{I}_{mn}$ constructed from these images can be written as

$$\underline{I}_{om} = \underline{P}_o \underline{P}_m^*, \quad \underline{I}_{on} = \underline{P}_o \underline{P}_n^*, \quad \underline{I}_{nm} = \underline{P}_n \underline{P}_m^* \tag{2}$$

where $\cdot^*$ denotes the complex conjugate. It can be shown that the phase of any of these interferograms can be obtained from the other two, e.g.,

$$\underline{\phi}_{nm} = W\{\underline{\phi}_{om} - \underline{\phi}_{on}\} \tag{3}$$

where $\underline{\phi}_{nm}$ is the wrapped interferometric phase of $\underline{I}_{nm}$ and $W\{\cdot\}$ is the wrapping (modulo-2π) operator. The equality of (3) is called the phase consistency or *phase triangularity* condition [18]. Note that the phase triangularity condition always holds by definition for single pixels, but it is not valid necessarily for multilooked interferometric pixels (see Fig. 1 as a numerical demonstration of the validity of the phase triangularity condition for single- and multilooked phases).

Under certain statistical conditions, the phase triangularity condition for multilooked pixels can be expressed in terms of phase expectation. Assuming a distributed scattering mechanism (i.e., each SAR pixel is a superposition of contributions from many elementary scatterers in a resolution cell), SLC pixels have a zero-mean multivariate circular Gaussian distribution [30], [31]. Under this assumption, the expectation of complex interferometric observations can be written as [32]–[34]

$$E\{\underline{I}_{nm}\} = S|\gamma_{nm}| \exp\left(j(\varphi_n - \varphi_m)\right) \tag{4}$$

where $E\{\cdot\}$ is the expectation operator, $|\gamma_{nm}|$ is the absolute value of normalized interferometric coherence, and

$S = \sqrt{E\{\underline{A}_n^2\}E\{\underline{A}_m^2\}}$. The phase terms $\varphi_n \in [-\pi, \pi)$ and $\varphi_m \in [-\pi, \pi)$ are the true phase values defined as the phase contributions related to the physical path difference between the target and the sensor (i.e., the phase contributions of deformation, topography, atmosphere, and orbital errors to the observed wrapped SLC phases). We rewrite (4) by adding and subtracting the true phase value of another image P_o from the argument of the complex interferogram $\underline{I}_{nm}$

$$E\{\underline{I}_{nm}\} = E\left\{\underline{A}_{nm} \exp(j\underline{\phi}_{nm})\right\}$$
$$= S|\gamma_{nm}| \exp\left(j(\varphi_n - \varphi_o - \varphi_m + \varphi_o)\right)$$
$$= S|\gamma_{nm}| \exp\left(j(\varphi_{om} - \varphi_{on})\right) \quad (5)$$

where φ_{om} and φ_{on} are now the true phase values of the interferometric phases and $\underline{A}_{nm}$ is the interferometric amplitude. If $\hat{\underline{\phi}}_{nm}$ denotes the multilooked phase, under the assumption that the signal components φ are constant within the averaging window, we obtain [33]

$$E\{\underline{\phi}_{nm}\} = E\{\hat{\underline{\phi}}_{nm}\} = W\{\varphi_{om} - \varphi_{on}\}. \quad (6)$$

In contrast to (3), we call (6) as the *expected phase triangularity* condition.

The term *SM-phase estimation* is defined as the estimation of a set of consistent interferometric phases (i.e., where the phase triangularity condition holds for every combination of three interferograms) from a stack of inconsistent multilooked interferograms. In other words, SM-phase estimation is the estimation of a deterministic signal φ from stochastic multilooked observations $\hat{\underline{\phi}}$ constrained by the phase triangularity condition. For simplicity, we omit the hat symbols $\hat{\phi}$, and we will use ϕ for multilooked phase in the remainder of this paper.

III. MATHEMATICAL MODEL FOR SM-PHASE ESTIMATION

A. Functional Model

For each pixel, assuming N radar images, the observation vector contains the available multilooked wrapped interferometric phases. In the most generic case where all of the interferometric combinations are used, the observation vector is an $N(N-1)/2$ vector of all multilooked wrapped interferometric phases ϕ_{nm}, where n and m are the radar image indices. The unknown parameters are the *true* SM wrapped interferometric phases φ_{oi}, where the o-index indicates the master acquisition. Then, (6) can be regarded as an observation equation with ϕ_{nm} as an observation and φ_{on} and φ_{om} as unknown parameters of interest. We reformulate (6) and write the nonlinear wrapping operator in a linear form by introducing an integer ambiguity term a_{nm} as

$$E\{\underline{\phi}_{nm}\} = \begin{cases} \varphi_{om} - \varphi_{on} + a_{nm}(2\pi) & \text{if } n, m \neq 0 \\ \varphi_{om} & \text{if } n = 0 \\ -\varphi_{on} & \text{if } m = 0 \end{cases} \quad (7)$$

where $a_{nm} \in \{-1, 0, 1\}$. Since the φ terms are wrapped phases, the value of $(\varphi_{nm} - \varphi_{on})$ can only lie between -2π and 2π,

and therefore, the ambiguity terms can only be 1, -1, or 0. In matrix notation, this linear system of observation equations is

$$E\left\{\begin{bmatrix} \underline{\phi}_{o1} \\ \vdots \\ \underline{\phi}_{o(N-1)} \\ \vdots \\ \underline{\phi}_{nm} \\ \vdots \end{bmatrix}_{y}\right\} = \underbrace{\begin{bmatrix} 0 & \cdots & 0 \\ \vdots & \ddots & \vdots \\ 0 & \cdots & 0 \\ 2\pi & & \\ & \ddots & \\ & & 2\pi \end{bmatrix}}_{A} \underbrace{\begin{bmatrix} \vdots \\ a_{nm} \\ \vdots \end{bmatrix}}_{a}$$

$$+ \underbrace{\begin{bmatrix} 1 & & \\ & \ddots & \\ & & 1 \\ \vdots & & \\ -1 \ldots 1 & \\ \vdots & & \end{bmatrix}}_{B} \underbrace{\begin{bmatrix} \varphi_{o1} \\ \vdots \\ \varphi_{o(N-1)} \end{bmatrix}}_{b} \quad (8)$$

where $n, m = 1 \ldots (N-1)$. Although the most generic case is presented here, in which all of the interferometric combinations are used, the model is flexible and can be written for any subset of interferograms. With model (8), we describe the SM-phase estimation problem in a hybrid system of linear equations with real unknowns φ_{on} and integer unknowns a_{nm}. The solution of this system of equations is given by ILS estimation.

IV. ILS

A. Estimator

Consider a system of linear observation equations with n integer and p real-valued unknown parameters

$$E\{\underline{y}\} = Aa + Bb \quad (9)$$

where $E\{\cdot\}$ is the expectation operator, $\underline{y} \in \mathbb{R}^m$ is the vector of observations, and $a \in \mathbb{Z}^n$ and $b \in \mathbb{R}^p$ are the vectors of integer and real-valued unknown parameters, respectively. The matrix $[A\ B]$ is given and assumed to be a full column rank matrix. Equation (9) is called the *functional model* as it describes the functional relation between the observations and the unknown parameters. The weighted ILS solution of (9) is

$$\check{a}, \check{b} = \arg\min_{a \in \mathbb{Z}, b \in \mathbb{R}} \|y - Aa - Bb\|_W^2 \quad (10)$$

where W is the weight matrix and $\|\cdot\|_W^2$ is a quadratic norm defined as $\|\cdot\|_W^2 = (\cdot)^T W(\cdot)$. The weight matrix W is used to assign different weights to different observations. In Section V-B, we discuss the implication of choosing a proper weight matrix for ILS SM-phase estimation. To account for the integer constraint of vector a, it is shown in [25] and [26] that

the objective function (10) can be orthogonally decomposed into the sum of three L_2-norm components

$$\|y - Aa - Bb\|_W^2$$

$$= \underbrace{\|y - A\hat{a} - B\hat{b}\|_W^2}_{1} + \underbrace{\|\hat{a} - a\|_{W_a}^2}_{2} + \underbrace{\|\hat{b}|_a - b\|_{W_b}^2}_{3} \quad (11)$$

where $\hat{a}$ and $\hat{b}$ are the real-valued unconstrained weighted least squares estimates of a and b vectors, and $b|_a$ is the conditional least squares estimates of vector b, conditioned on a. The matrices W_b and W_a are defined as

$$W_b = B^T W B \quad (12)$$

$$W_a = F^T W F \quad (13)$$

where

$$F = A - B(B^T W B)^{-1} B^T W A. \quad (14)$$

Because of the orthogonality condition among the three L_2-norm components, as soon as $\hat{a}$ and $\hat{b}$ are computed using ordinary least squares, the minimization problem (10) can be regarded as two individual minimization problems of

$$\check{a} = \arg\min_{a \in \mathbb{Z}} \|\hat{a} - a\|_{W_a}^2 \quad (15)$$

$$\check{b} = \arg\min_{b \in \mathbb{R}} \left\|\hat{b}|_a - b\right\|_{W_b}^2. \quad (16)$$

As a consequence, the solution of (10) can be derived in three steps as follows [24].

1) The standard weighted least squares estimation is performed by disregarding the integer constraint $a \in \mathbb{Z}^n$ in order to compute $\hat{a}$ and $\hat{b}$

$$\begin{bmatrix} \hat{a} \\ \hat{b} \end{bmatrix} = \left([A\ B]^T W [A\ B]\right)^{-1} [A\ B]^T W y. \quad (17)$$

These solutions are called *float solutions*.

2) To solve the minimization of (15), integer unknowns in vector $\check{a}$ are estimated by mapping the float solution $\hat{a}$ to the corresponding integer (fixed) solution using a mapping operator $S : \mathbb{R}^n \mapsto \mathbb{Z}^n$, i.e., $\check{a} = S(\hat{a})$. In this mapping, the float solution vector $\hat{a}$ is mapped to the *nearest* integer vector. However, *nearest* must be measured in the metric of matrix W_a in order to account for the correlation among float solutions in vector $\hat{a}$.

To estimate $\check{a}$, there exist two common integer estimators. The *ILS* estimator accounts for all of the correlation among float solutions, and the *integer bootstrapping* (IB) estimator considers some of the correlations among the entries of $\hat{a}$. Although the ILS estimator is more optimal, its solution cannot be given in a closed form, and its computational time is larger compared to the bootstrapping method. Here, we use the bootstrapping approach. A detailed explanation of these algorithms can be found in

[25] and [26]. We also briefly describe the bootstrapping algorithm in Appendix A.

3) Solving the minimization (16) is the most straightforward as it is a well-determined problem (same number of unknowns as equations). Therefore, in principle, the solution is given as

$$\check{b} = \hat{b}|_a. \quad (18)$$

However, the true value a is unknown. Assuming that $\check{a}$ is the correct estimation of a, we have $a = \check{a}$. Based on this assumption, once the fixed solution $\check{a}$ is obtained, the fixed solution of real parameters $\check{b}$ is computed as

$$\check{b} = \hat{b}|_{\hat{a}} = \left(B^T W B\right)^{-1} B^T W (y - A\check{a}). \quad (19)$$

Assuming Q_y as the covariance matrix of observation vector y, the covariance matrix of the fixed solution $\check{b}$ can be also obtained as

$$Q_{\check{b}} = Q_{\hat{b}|_{\hat{a}}} = (B^T W B)^{-1} B^T W Q_y W B (B^T W B)^{-1}. \quad (20)$$

Note that, although we formulate the ILS problem with a generic weight matrix W (not with $W = Q_y^{-1}$), however, we use the phase covariance matrix in (20) to propagate the dispersion of observations to the final estimates and to obtain $Q_{\check{b}}$, which is a full covariance matrix describing the precision of the estimated phases.

V. APPLICATION OF ILS FOR SM-PHASE ESTIMATION

Having the functional model (8) for each pixel in an interferogram stack, the three ILS steps can be applied to estimate the SM wrapped interferometric phases. For (17), (19), and (20), two more ingredients are required: the covariance matrix of the phase observations Q_y and the proper weight matrix W. In the following, we address these two elements with some more practical considerations. Note that the observation covariance matrix Q_y is not needed for SM-phase estimation, and it is required only for computation of the precision of the estimates via (20).

A. Covariance Matrix of Interferometric Phase Stack

The second central statistical moment of the interferometric phases in vector $\underline{y}$ is described via the covariance matrix Q_y with a maximum size of $N(N - 1)/2$ when all possible interferometric pairs are used. Although the closed-form expression of interferometric phase variances (i.e., diagonal elements of Q_y) for the single-looked interferograms was presented in [31] and [34], there is no closed-form evaluation for multilooked cases and for off-diagonal covariance elements in Q_y. Here, we propose a numerical Monte Carlo approach to evaluate the full covariance matrix of an interferogram stack.

It is assumed, based on the central limit theorem, that the real and imaginary values in an SLC stack have a multivariate circular Gaussian distribution with zero mean, a zero correlation between the real and imaginary parts, and a variance proportional to the average radar cross section of the surface

[32], [35]. Considering a stack of N SLC images, the vector of real and imaginary values for pixel k is

$$y_{\mathrm{slc}_k} = \left[\mathrm{Re}_k^0 \cdots \mathrm{Re}_k^{(N-1)} \mathrm{Im}_k^0 \cdots \mathrm{Im}_k^{(N-1)} \right]^T \quad (21)$$

where y_{slc_k} has a multivariate circular Gaussian distribution with PDF [36]

$$\mathrm{pdf}_{\underline{y}_{\mathrm{slc}_k}}(y_{\mathrm{slc}_k}) = \frac{1}{(2\pi)^3 D^{\frac{1}{2}}} \exp\left(-\frac{1}{2} y_{\mathrm{slc}_k}^T D^{-1} y_{\mathrm{slc}_k} \right). \quad (22)$$

D is a $2N \times 2N$ covariance matrix given by (assuming zero-mean phase)

$$D = \begin{bmatrix} C & 0 \\ 0 & C \end{bmatrix} \quad (23)$$

where C is the $N \times N$ absolute coherence matrix of y_{slc_k}. Note that, in this formulation, the amplitude of SLC images is assumed to be normalized (i.e., $E\{\underline{A}_m^2\} = 1$). The elements of C are the absolute interferometric coherences (i.e., $C_{nm} = |\gamma_{nm}|$). If we assume that the coherence matrix C has already been computed for each pixel, we generate a large number ($M \times L$) of samples $y_{\mathrm{slc}_k}^{(i)}$, $i = 1, \ldots, M \times L$, from $\mathrm{pdf}_{\underline{y}_{\mathrm{slc}_k}}(y_{\mathrm{slc}_k})$, where L is the known number of looks and M is the number of desired realizations of the phase observation vector. From this set of SLC samples, we compute M realizations $y_k^{(i)}$, $i = 1, \ldots, M$, of the vector of multilooked interferometric phases (i.e., for each realization, the multilooked vector y_k is computed from L samples of y_{slc_k}). The covariance matrix Q_{y_k} for the pixel k is estimated by averaging the M empirical covariance matrices as [37]

$$Q_{y_k} = \frac{1}{M} \sum_{i=1}^{M} \left(y_k^{(i)} - E\{\underline{y}\} \right) \left(y_k^{(i)} - E\{\underline{y}\} \right)^T \quad (24)$$

where $E\{\underline{y}\}$ is computed as the average of all $y_k^{(i)}$ samples. In this way, given the coherence matrix C, the full covariance matrix Q_y can be computed.

Assuming a large number of pixels, it is clear that this approach is computationally expensive to be applied for every pixel in large stacks. To solve this problem, we calculate once the covariance values for all possible coherence combinations and for all different multilooking factors, and store the results in a multidimensional lookup table indexed by coherences and multilooking factors. Therefore, in practice, instead of applying the Monte Carlo simulation for each pixel, the elements of the covariance matrix are taken from the lookup table.

B. Choice of Weight Matrix

The ILS problem has been conventionally formulated with a weight matrix equal to the inverse of the covariance matrix of the observations. This is logical for observations with a Gaussian distribution because using $W = Q_{\underline{y}}^{-1}$ provides the maximum likelihood (ML) estimation. As the multilooked interferometric phases are not normally distributed, their data statistics cannot be explained fully by the phase covariance

matrix. Also, an accurate covariance matrix may not always be available. Therefore, we express ILS with a generic weight matrix W, increasing the flexibility of the method to digest different kinds of weight matrices.

Focusing on the fundamental difference between non-Gaussian random variables (such as interferometric phases) and Gaussian variables: while, for the latter, the variance/dispersion is truly the measure of information loss (as the PDF of Gaussian variables can be completely characterized by the dispersion or the covariance matrix in multivariate cases), for interferometric phases, the variance is always bounded and is not representative of information loss. In fact, a zero coherence interferometric phase conveys no information (corresponding to information loss of ∞), while its variance is equal to $(2\pi)^2/12$, which is the variance of uniformly distributed phase between $-\pi$ and π.

In the case of SM-phase estimation, a reasonable choice for weighting the observations is the coherence of each interferometric phase in vector y. In this case, W is defined as a diagonal matrix in which the weight of an observation $\underline{\phi}_{mn}$ is defined as

$$w_{\underline{\phi}_{mn}} = \gamma_{mn} \quad (25)$$

where γ_{mn} is the absolute coherence value.

Another weighting strategy is based on the information content of interferometric multilooked phases. A common measure of information content of a random variable about an unknown parameter is the *Fisher information* index [38]. If we consider φ_{mn} to be the expected interferometric phase of the multilooked observation $\underline{\phi}_{mn}$, the amount of information included in $\underline{\phi}_{mn}$ about φ_{mn} can be quantified by the Fisher information index of interferometric phase as [39]

$$\mathcal{I}_{\underline{\phi}_{mn}}\{\varphi_{mn}\} = \frac{2L\gamma_{mn}^2}{1 - \gamma_{mn}^2} \quad (26)$$

which results in zero information for $\gamma_{mn} = 0$ and maximum information of infinity when $\gamma_{mn} = 1$. In other words, $\mathcal{I}_{\underline{\phi}_{mn}}\{\varphi_{mn}\}$ accounts for the loss of information about φ_{mn} due to the noise and decorrelation. Therefore the diagonal elements of a Fisher-information-based W matrix is defined as

$$w_{\underline{\phi}_{mn}} = \mathcal{I}_{\underline{\phi}_{mn}}\{\varphi_{mn}\}. \quad (27)$$

In Section VI-B3, we compare the influence of different weighting strategies on the efficiency of ILS SM-phase estimation.

C. Practical Considerations

With the functional model of (8), the covariance matrix of (24), and the weight matrix of (27), we have all of the required ingredients to apply ILS. Here, we list some practical considerations for the proposed SM-phase estimation.

1) *Float solution*: In (8), if all of the SM interferograms are included in the observation vector y, the numbers of equations and unknowns are equal, and hence, the solution of the first ILS step (i.e., float solution) can be simply computed as

$$\begin{bmatrix} \hat{a} \\ \hat{b} \end{bmatrix} = [A\ B]^{-1} y. \quad (28)$$

However, if we use a smaller subset of interferograms and if this subset does not include all of the SM interferograms, the number of unknowns will exceed the number of equations, and the float solution is not computable as the matrix $[A\ B]$ is rank deficient and not invertible. As a consequence, the limitation of the proposed model is that the subset should always include all of the SM interferograms. If some of the SM interferograms are not available, pseudo-observations can be introduced in the model to overcome rank deficiency.

2) *Statistical homogeneity of the averaging area*: The multilooked phases in vector y are computed by spatial averaging over statistically homogeneous pixels (SHPs). In order to satisfy the homogeneity condition, we use a spatially adaptive averaging window. In [18], a space adaptive filtering algorithm has been introduced in order to, for each pixel, define a *brotherhood area* including neighboring SHP based on Kolmogorov–Smirnov test. Alternative approaches with different tests and implementations are also given in [40]–[44]. To reduce the influence of nonhomogeneous pixels (outliers) in the averaging areas, the concept of robust coherence estimation can be also used [45].

3) *Signal consistency in the averaging area*: Another assumption in the computation of multilooked phases y for each pixel is that the signal components of φ are constant in the averaging area. This assumption is reasonable for relatively small areas with spatially correlated signals. However, if a high spatial variation of signal components is expected, this phase variation should be removed beforehand. Examples of variable signals are high topography gradient or orbital errors. These kinds of spatially variable signals can be removed by different kinds of phase flattening or low-pass filters such as the adaptive multiresolution defringe algorithm in [41], [43], and [46], patch detrending in [31] and [47], or low-pass filtering in [5].

4) *Posterior assessment*: After SM-phase estimation, the quality of the estimated phase values should be assessed. In [18], an extended temporal coherence $\hat{\gamma}_{\mathrm{PTA}}$ has been introduced as a goodness-of-fit measure for SM-phase estimation. This parameter can be written in our model notation as

$$\hat{\gamma}_{\mathrm{PTA}} = \left| \frac{1}{N_{\mathrm{ifgs}}} H^T \exp\left(j(y - B\check{b}) \right) \right| \qquad (29)$$

where j is the imaginary unit, N_{ifgs} is the number of interferograms in the stack, and H is an all-ones column vector with a length of N_{ifgs}. If all of the possible interferometric combinations are used, $N_{\mathrm{ifgs}} = N(N-1)/2$. The coherence $\hat{\gamma}_{\mathrm{PTA}}$ is used for the final selection of DS with reliable phase estimation.

VI. Synthetic Data Processing

In order to validate the ILS SM-phase estimation and evaluate its performance, we test it on a set of synthetic datasets. Here, we describe the simulation settings, followed by results and discussion.
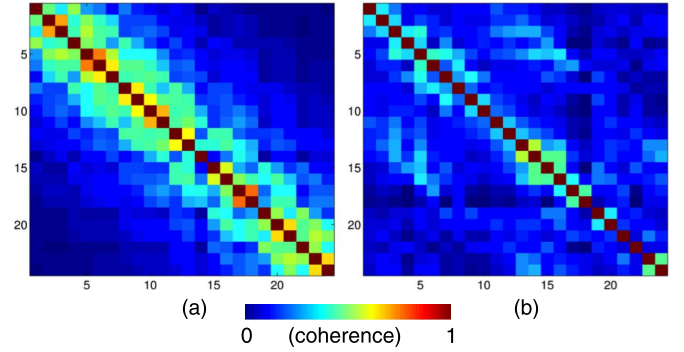

Fig. 2. Coherence matrices of the synthetic data for two scenarios. (a) Exponential decay C_e. (b) Seasonal decay C_s. The images are ordered based on their acquisition dates equidistantly spaced in time with a revisit time of 35 days.

A. Simulation Setting

We generated two radar data stacks with different noise behaviors. Each dataset included 24 SLC images with a revisit time of 35 days. A deformation signal was simulated by assuming a simple Gaussian deformation bowl with a maximum line-of-sight (LOS) deformation rate of 3 cm/year at the center and a radius of 600 m. We assumed a flat area, resulting in a zero topographic signal. The atmospheric signal was simulated by assuming the power law behavior presented in [48]. A crop of 1000×1000 m, a radar wavelength of 56 mm, and a pixel size of 20×20 m were also assumed. For noise simulation, we assume that all of the pixels have the same statistics. The noise components are simulated based on the assumption of a zero-mean multivariate circular Gaussian distribution. In this way, for noise simulation, only a coherence matrix is required [see (22)]. In this paper, we have assumed two arbitrary scenarios for temporal decorrelation: exponential decay and seasonal decay. The coherence matrices are constructed for the two scenarios as explained in Appendix B and shown in Fig. 2. The noise time-series of each pixel is simulated by generating a random vector of complex numbers which have a multivariate zero-mean circular Gaussian distribution with the associated coherence matrix. The noise-free and noisy simulated datasets are visualized in Figs. 4 and 5(a) and (b), respectively.

B. Simulation Results

We first analyze the overall results before diving into specific aspects that influence the simulation results.

1) Overall Analysis: We applied the ILS SM-phase estimation on the two simulated datasets. In order to construct the observation vector y for each pixel, the simulated phases were multilooked by coherent phase averaging over 5×5 windows. As discussed in Section V-C, to meet the signal consistency assumption in the averaging windows, the spatially variable signal within an averaging area should be removed by a defringing/detrending algorithm. In this simulation, in order not to be affected by the suboptimality of detrending algorithms, the spatially variable signal (or the trend) in the averaging windows is computed and corrected based on the known noise-free simulated signal. The weight matrix for each dataset is constructed using the Fisher information of multilooked phases computed
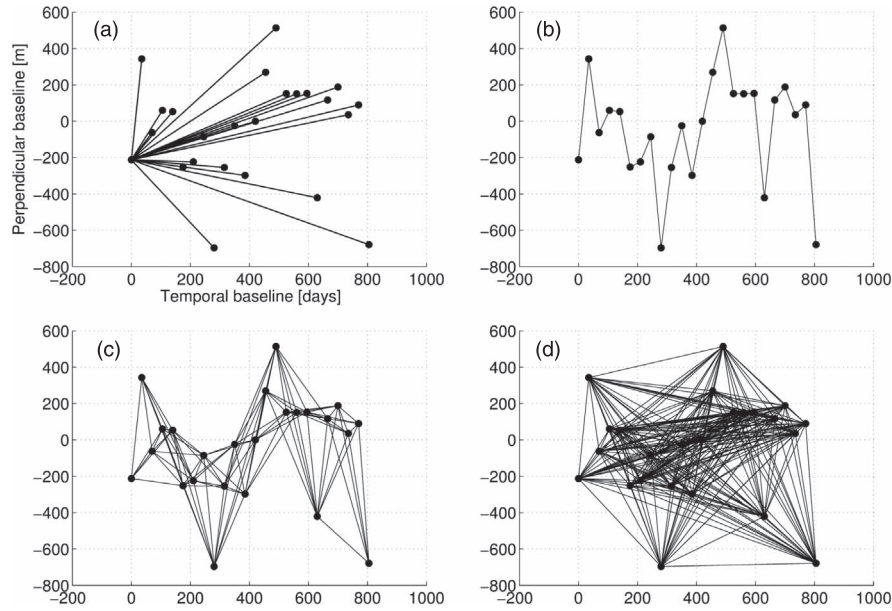
Fig. 3. Example of baseline configurations used in the synthetic experience. (a) Single master (SM). (b) STBs. (c) SB subset (SB). (d) All interferometric combinations.
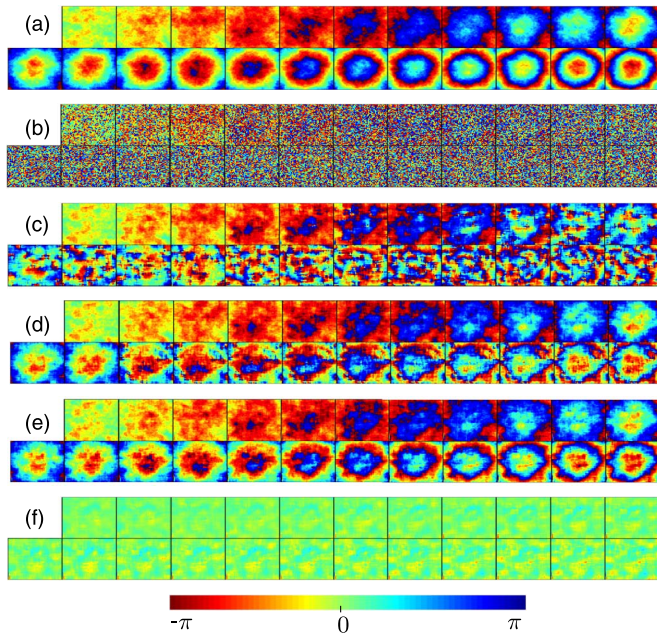

Fig. 4. Synthetic example (exponential-decay scenario). (a) Simulated signal (deformation and atmosphere) for SM interferograms using the first acquisition as the master image. (b) Interferograms after adding decorrelation noise. (c) SM interferograms after multilooking. (d) Reconstructed SM interferograms from consecutive multilooked STB interferograms. (e) Results of the ILS method using all interferograms. (f) Residuals of the ILS method [i.e., the difference between subfigures (a) and (e)].
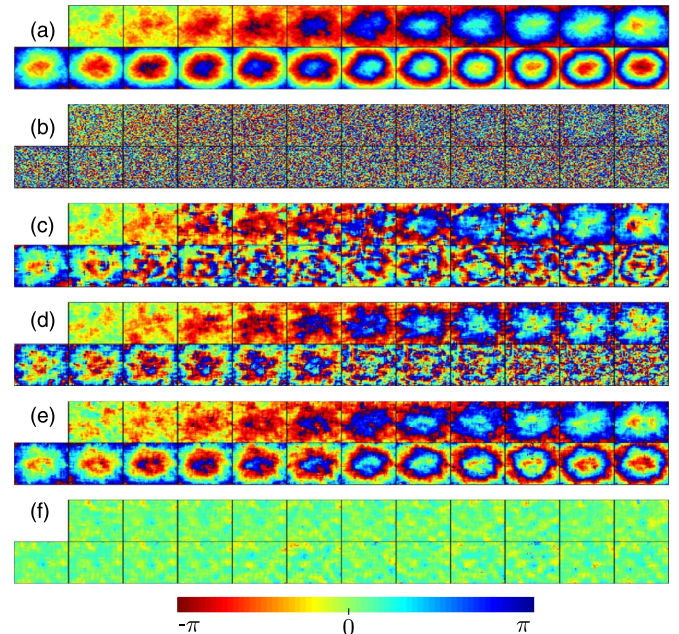
Fig. 5. Synthetic example (seasonal-decay scenario)—simulated data results. (a) Simulated signal (deformation and atmosphere) for SM interferograms using the first acquisition as the master image. (b) Interferograms after adding decorrelation noise. (c) SM interferograms after multilooking. (d) Reconstructed SM interferograms from consecutive multilooked STB interferograms. (e) Results of the ILS method using all interferograms. (f) Residuals of the ILS method [i.e., the difference between subfigures (a) and (e)].

from the true coherence values based on (27). To provide a generic comparison with conventional *ad hoc* phase retrieval methods, we also examined the SM-phase construction by multilooking the original (SM) interferograms [Fig. 3(b)] and by consecutive integration of the temporally adjacent multilooked interferograms, denoted as the small temporal baseline (STB) configuration [see Fig. 3(b)]. The results are summarized in Figs. 4 and 5 for the two scenarios. Figs. 4 and 5(a) and (b) show

the noise-free and noisy simulated SM-phases, respectively. Figs. 4 and 5(c) show the reconstructed phases computed by multilooking the original SM-phases, and Figs. 4 and 5(d) show the reconstructed phases from STB interferograms. The results of ILS SM-phase estimation using all of the interferograms [i.e., the baseline configuration in Fig. 3(d)] are presented in Figs. 4 and 5(e). Finally, the difference between the original simulated signal and the ILS estimates is plotted in Figs. 4 and 5(f).

(a) exponential decay scenario
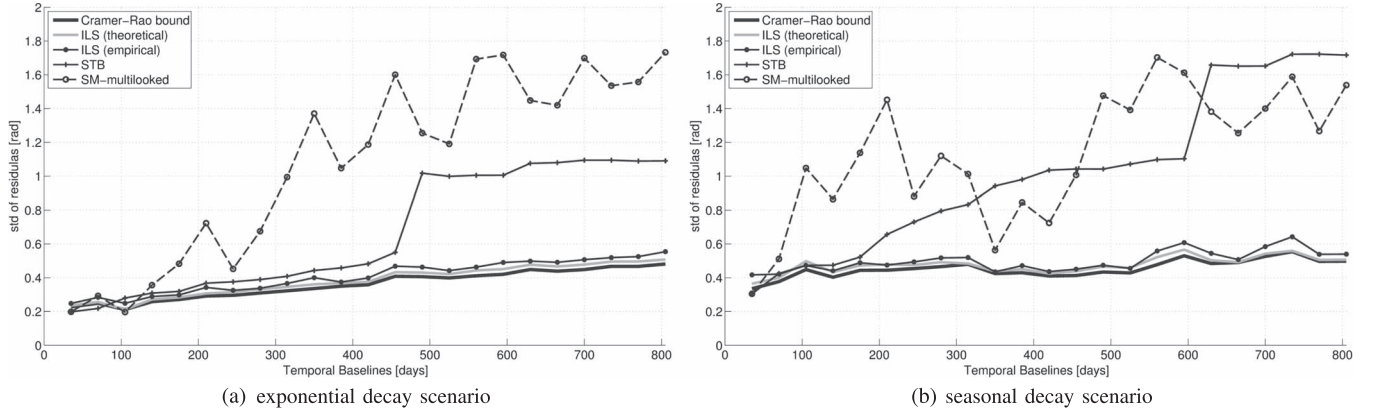
(b) seasonal decay scenario

Fig. 6. Empirical standard deviation of the residuals for three different reconstruction approaches (the multilooked SM stack, the STB reconstructed stack, and the ILS SM-phase estimation for the two simulation scenarios). (a) Exponential decay. (b) Seasonal decay. For comparison, we also plotted the theoretical standard deviation computed as square root of the diagonal elements of $Q_{\hat{b}}$ and also the lower CRB of SM-phase estimation. In both scenarios, the results of the ILS SM-phase estimation outperform the STB and SM reconstruction methods. There is a good agreement between the theoretical and empirical standard deviations. The empirical standard deviations are close to CRB, indicating the efficiency of the ILS SM-phase estimation.

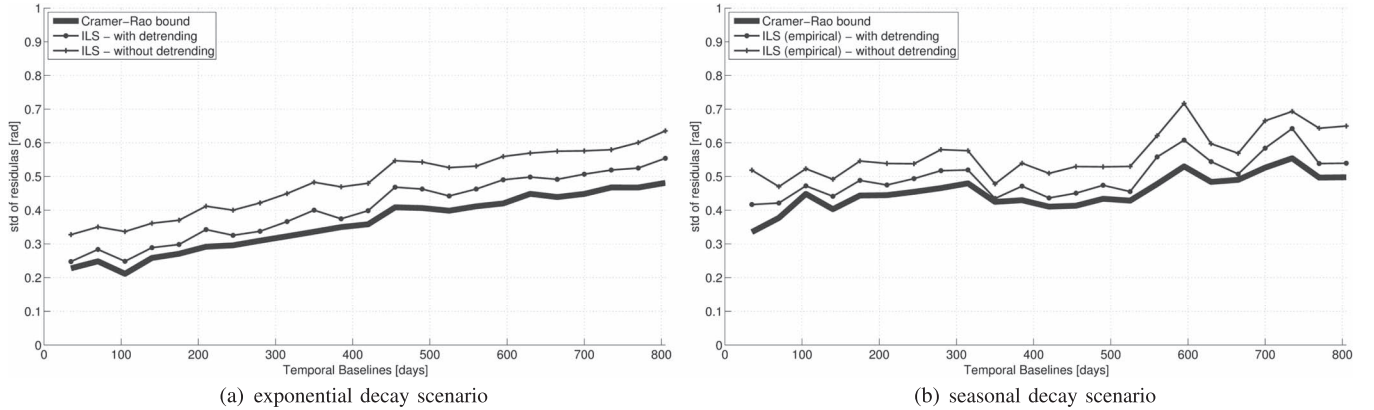(a) exponential decay scenario

(b) seasonal decay scenario

Fig. 7. Effect of the nonstationary signal within averaging windows on the empirical standard deviation of the residuals for (a) exponential decay and (b) seasonal decay. For comparison, we also plotted the lower CRB of SM-phase estimation.

Initial qualitative evaluation shows that, in both scenarios, ILS can effectively filter out noise and is able to reconstruct the original signal. The results indicate better phase reconstructions than SM and STB methodologies, demonstrating the generic added value of using the SM-phase estimation procedure. In both scenarios, the residuals between the ILS-reconstructed signal and the true signal have a zero mean, indicating an unbiased estimation.

Fig. 6(a) and (b) provides a more quantitative evaluation. We calculated the standard deviation of the residuals (i.e., the difference between the constructed interferograms and the true values) for the multilooked SM, the STB reconstructed, and the ILS estimated stacks. For comparison, we also computed the theoretical standard deviations of ILS results from diagonal elements of $Q_{\hat{b}}$ [see (20)]. To assess the efficiency of the ILS estimator, we also calculated the lowest achievable standard deviation as the square root of the CRB for SM-phase estimation [17].

In both scenarios, we see that the results of ILS SM-phase estimation outperform the STB and SM reconstruction methods. The residual standard deviations of the STB reconstruction increase with temporal baseline because of the accumulation of noise in the reconstruction process. For SM multilooking, as

expected, the standard deviations are variable and dependent on the coherence level; the higher the coherence, the lower the phase standard deviation. For ILS, there is a good agreement between the theoretical and empirical standard deviations. Note that, in general, for Gaussian observations, least squares is a minimum-variance estimator, and its variance is equivalent to the CRB. However, interferometric phases are not Gaussian, and empirical standard deviations are hence compared with the analytical CRB. In both scenarios, the empirical standard deviations approach the CRB with an average difference of ~0.07 rad or $4°$ (equivalent to 0.3 mm for C-band), which is negligible compared to the standard deviation expected for high-SNR point targets. The closeness to the CRB is an indicator of the efficiency of the ILS estimator.

2) On the Influence of the Nonstationary Signal Within Averaging Windows: As mentioned before, we computed and corrected for the spatially variable signal (trend) in the multilooking windows using the known noise-free simulated signal. To evaluate the effect of the trend on the efficiency of SM-phase estimation, we applied the ILS estimation on both of the detrended dataset and the one with the trend included. The results are summarized in Fig. 7. We observe that trend removal
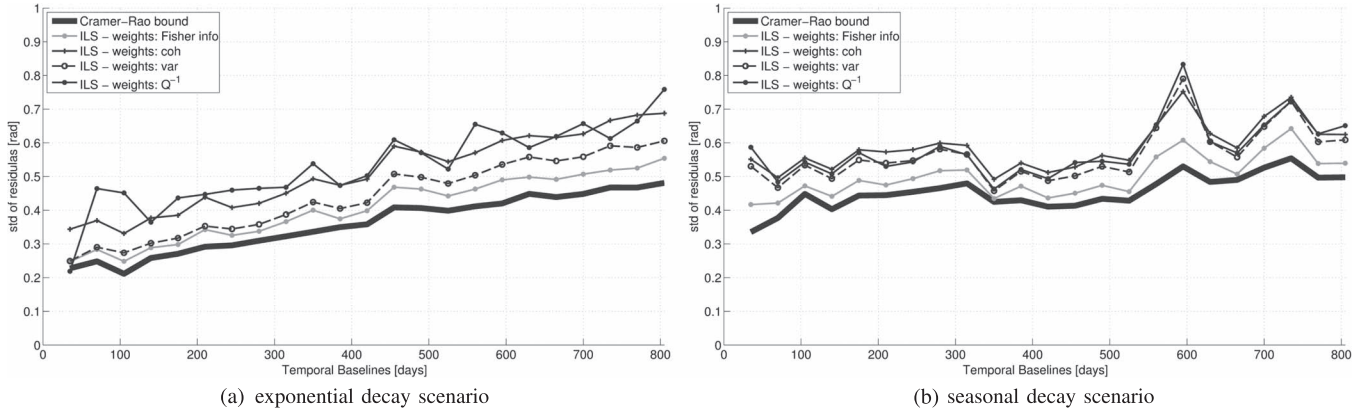
Fig. 8. Effect of assigned weights on empirical standard deviation of the residuals for (a) exponential decay and (b) seasonal decay. For comparison, we also plotted the lower CRB of SM-phase estimation.
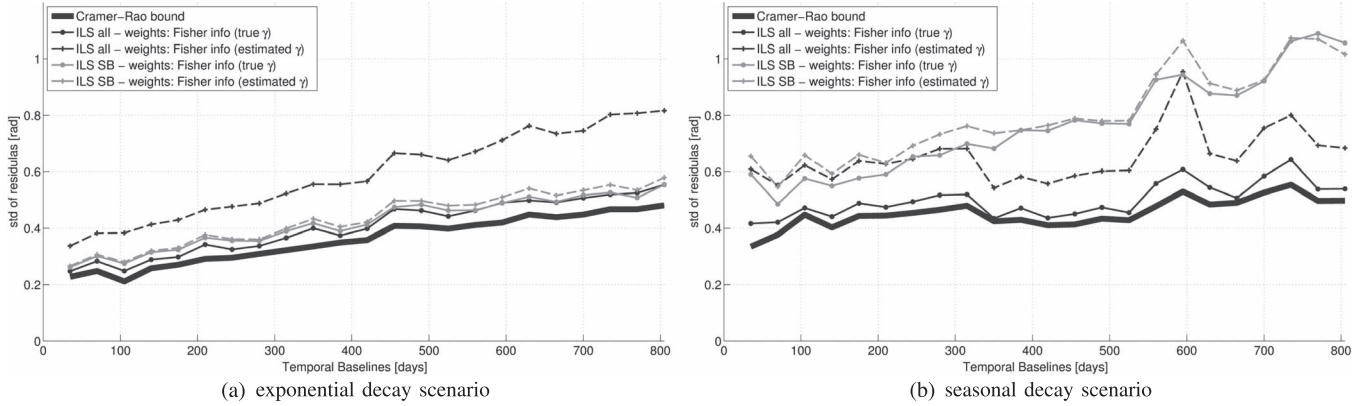

Fig. 9. Effect of coherence bias and using interferogram subsets for two simulation scenarios. (a) Exponential decay. (b) Seasonal decay.

reduces the standard deviation of the residuals significantly. The ratio between the CRB and the standard deviations is approximately two times smaller for the detrended datasets. This indicates the importance of applying a defringing/detrending algorithm during the multilooking/averaging process.

3) On the Influence of Assigned Weights: We applied ILS SM-phase estimation on the two simulated scenarios with four different weighting strategies (see Section V-B): setting W as the inverse of the observation covariance matrix (i.e., $W = Q_y^{-1}$), with diagonal elements as inverse variance, coherence, and Fisher information index, respectively. The resulting effects on the precision of the phase estimation are summarized in Fig. 8. We observe that the Fisher-information-based weight matrix is the most efficient. This demonstrates that the dispersion-based weighting strategies (i.e., the inverse of the covariance matrix or the inverse of the variances) are not optimal for multilooked phase observations, which have a non-Gaussian distribution. In other sections of this paper, we only show the results of ILS estimation based on the Fisher information weighting strategy.

4) On the Influence of Coherence Bias and Interferogram Selection: It may be observed that all of the aforementioned weighting strategies require coherence values for calculating W. The coherence values for each pixel can be practically computed from interferograms by spatial coherent averaging [39], [48]. It has been shown that the estimated coherence is biased, particularly for low coherence and small averaging areas [31], [34], [47]–[51]. Increasing the number of looks reduces this bias. Here, we evaluate the effect of the coherence bias on estimation precision. We applied ILS SM-phase estimation using the Fisher-information-based weight matrix computed both from the true (i.e., the one used in the simulation) and estimated coherence values. The results are shown in Fig. 9(a) and (b). In addition to using all of the interferometric combinations, we also applied the ILS estimation on an SB subset (SB) of interferograms. Fig. 3(c) and (d) demonstrates the baseline configuration for SB and all interferograms, respectively. We notice that, in both scenarios, using all of the interferograms with the true coherence gives the best results. When using all of the interferograms with the estimated coherences, the precision deteriorates (approximately with a factor of 2) due to the biased coherence estimation. However, in case of SB, there is no significant difference between using the true or estimated coherences in the weight matrix. This is because we only use interferograms with relatively high coherence (i.e., a low bias in the coherence estimation), and hence, the results are minimally affected by the coherence bias. We also observe that, in the exponential-decay scenario [Fig. 9(a)], using the
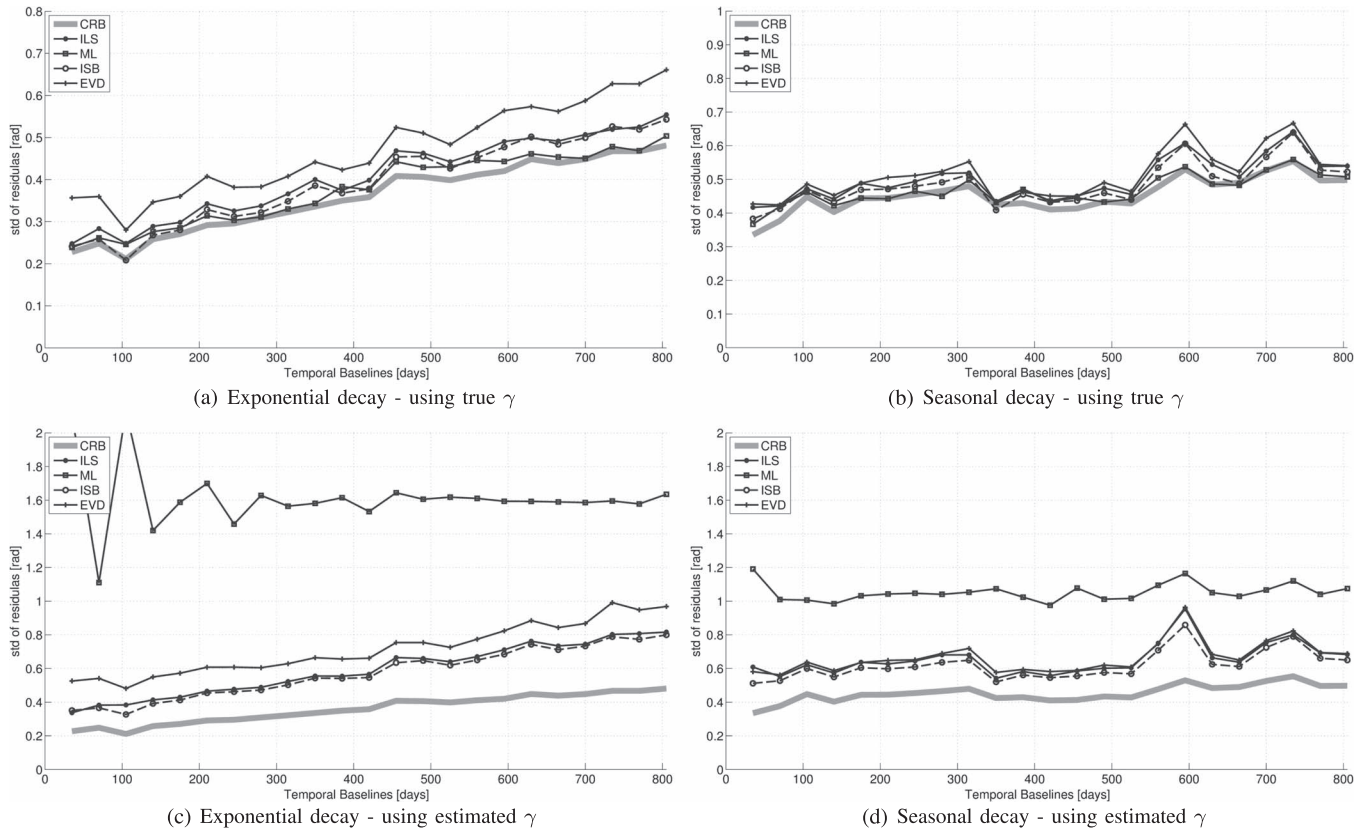
Fig. 10. Empirical standard deviation of the residuals for different SM-phase estimation methodologies. (a) Exponential-decay scenario with true coherence values. (b) Seasonal-decay scenario with true coherence values. (c) Exponential-decay scenario with estimated coherence values. (d) Seasonal-decay scenario with estimated coherence values. For comparison, the lower CRB of SM-phase estimation is also plotted. (a) Exponential decay—using true γ. (b) Seasonal decay—using true γ. (c) Exponential decay—using estimated γ. (d) Seasonal decay—using estimated γ.

SB subset provides results with the same precision as using all of the interferograms with the true coherences. This is, in fact, expected because, in this scenario, the large temporal baseline interferograms have zero coherence and do not convey any information and hence do not have any added value on the estimation efficiency. This is an important conclusion: for SAR stacks with a large number of images, where the computation of all of the interferometric combinations can be cumbersome, using an SB subset of interferograms can provide the same phase precision for SM-phase estimation as using the set of all of the interferograms. It should be noted, however, that selecting the most informative subset of interferograms is a challenging task and no generic methodology exists, as it requires *a priori* knowledge on the coherence behavior of DS targets.

5) Comparison With Other SM-Phase Estimation Methods: In this section, we compare the results of the ILS method with the results obtained by application of three other SM-phase estimation methodologies on the two synthetic datasets. These three methodologies are the following:

1) the ML SM-phase estimation used in the phase-linking method [17] and SqueeSAR [18];
2) the SM-phase estimation methods based on eigenvalue decomposition (EVD) of the full complex coherence matrix, as in the CAESAR algorithm [20] and in [21];

3) the SM-phase estimation method based on the minimization of the weighted circular variance of the complex interferometric residuals, presented in the framework of an improved-SBAS (ISB) algorithm [19].

The first two methods (ML and EVD) exploit the full complex coherence matrix, and hence, they use all of the interferometric combinations. For a fair comparison, we use all of the interferometric combinations for both ILS and ISB as well. To study the influence of biased coherence estimation on the efficiency of different methods, we apply all of the methods both with the true absolute coherences and with the estimated coherences. Fig. 10 shows the results of this comparison. Using the true coherence values [Fig. 10(a) and (b)], all of the methods show comparable performance. Using the true coherence values, the ML method gives the most efficient results, approaching the CRB. The ILS and ISB methods show comparable efficiency, which is slightly lower than the ML estimation, and EVD provides the lowest efficiency. However, when we look at the results based on the estimated coherences [Fig. 10(c) and (d)], the results vary significantly, showing different sensitivities of the methods to the biased estimation of coherence values. The ML estimator is affected the most by the biased coherences. This is logical as the ML is the only estimator that requires the inversion of the coherence matrix, and hence, small numerical biases in coherence estimation are amplified during the matrix

TABLE I
COMPARISON OF THE COMPUTATION TIME (IN SECONDS) OF
DIFFERENT SM-PHASE ESTIMATION METHODS APPLIED
ON THE TWO SIMULATION SCENARIOS

Method	ILS	ML	ISB	EVD
Exponential decay scenario	42.1	6.2	6.2	2.8
Seasonal decay scenario	42.5	6.3	6.4	3.1

inversion and severely affect the estimation efficiency. In fact, it has been discussed in the SqueeSAR algorithm that the estimated coherence matrix is not, in general, positive definite and is ill-conditioned, requiring the use of a pseudoinverse or a damping factor before the matrix inversion [18]. In our implementation of ML estimation, we use the pseudoinverse. Among other methods, when using estimated coherences, ILS and ISB show comparable results, and once again, EVD provides a relatively low efficiency.

To summarize, the results show that the ILS and ISB methods provide comparable efficiency, and they are less sensitive to the biased estimation of coherence values. Even though the ML estimation is theoretically the most efficient method, it is severely affected by biased coherence estimation and numerical instabilities in the matrix inversion. Generally, EVD shows a lower efficiency than the ILS and ISB methods. However, EVD has an additional functionality compared to the other methods. In case of DS with multiple scattering mechanisms, recent studies have showed that EVD is capable of decomposing the contribution of different mechanisms [20], [21], [52]. However, in our specific simulation based on a single scattering mechanism, the efficiency of EVD is lower than the other methods.

In addition to the different estimators considered in our simulation, a relatively new mathematical framework has been introduced for robust parameter estimation in InSAR stacks [45]. This approach has added value for non-Gaussian data which are also contaminated with outliers. In principle, the proposed robust framework can be applied on all of the aforementioned SM-phase estimators, including ILS. This study aims to introduce a new estimator and provide a proof of concept for ILS SM-phase estimation; further comparison between different estimators and their robust implementation is beyond the scope of this study.

Regarding computational time of different methods, it is difficult to give an accurate and fair analysis as it strongly depends on the implementation of the different methods. An indication of the relative computational times of different estimators applied on the simulation of this study is summarized in Table I. We see that the main drawback of ILS with respect to other estimators is its high computational time, which is approximately seven times higher than the ML and ISB methods in our implementation. In this context, recent advances in the implementation of fast ILS estimation algorithms, e.g., [53], can be considered.

6) On the Posterior Assessment of the Results: Fig. 11 shows the temporal coherence $\hat{\gamma}_{\text{PTA}}$ [see (29)] for both simulation scenarios. A low value of $\hat{\gamma}_{\text{PTA}}$ indicates a large disagreement between the observations and the estimated parameters and so unreliable SM-phase estimation. The source of these large residuals can be related to the erroneous estimation of ambiguities in the second step of ILS SM-phase estimation. When
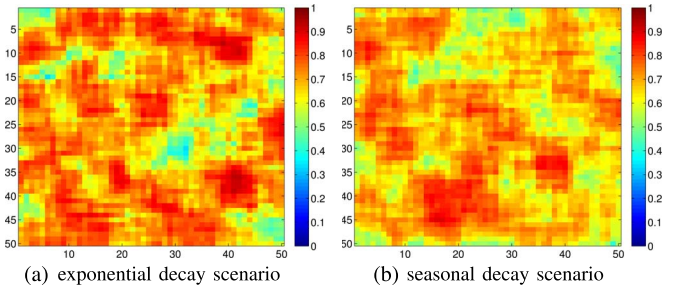

Fig. 11. Temporal coherence $\hat{\gamma}_{\text{PTA}}$ for the two simulation scenarios: (a) exponential decay and (b) seasonal decay, over the simulated area of 50×50 pixels.
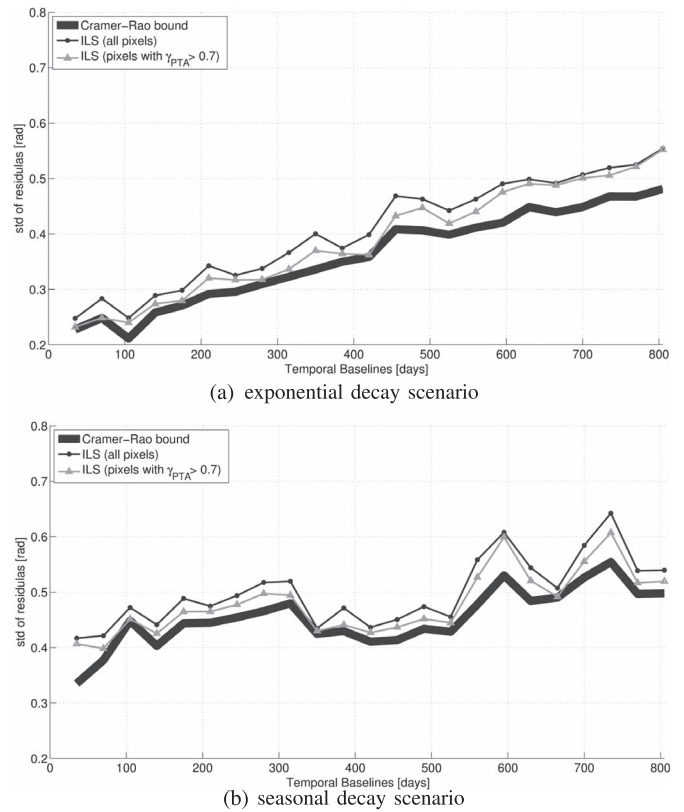

Fig. 12. Effect of the exclusion of unreliable estimates with $\hat{\gamma}_{\text{PTA}} < 0.7$ on the final precision of ILS SM-phase estimation for the two simulation scenarios. (a) Exponential decay. (b) Seasonal decay. By excluding the unreliable pixels, the standard deviations are reduced and approaching the CRB, confirming that the extended temporal coherence $\hat{\gamma}_{\text{PTA}}$ can be used effectively for the final selection of DS with reliable phase estimation.

ambiguities are mapped to the wrong integers, the quality of the final estimation will be lower, and it will result in a low $\hat{\gamma}_{\text{PTA}}$. Therefore, by excluding the pixels with low $\hat{\gamma}_{\text{PTA}}$, we can remove unreliable pixels with erroneous SM-phase estimation. Fig. 12 shows the effect of this exclusion on the final precision. The threshold of $\hat{\gamma}_{\text{PTA}} < 0.7$ was used to exclude unreliable estimates. We can see that the standard deviations were reduced and they approach the CRB. These results confirm that the temporal coherence $\hat{\gamma}_{\text{PTA}}$ can be used effectively for the final selection of DS with reliable phase estimation.
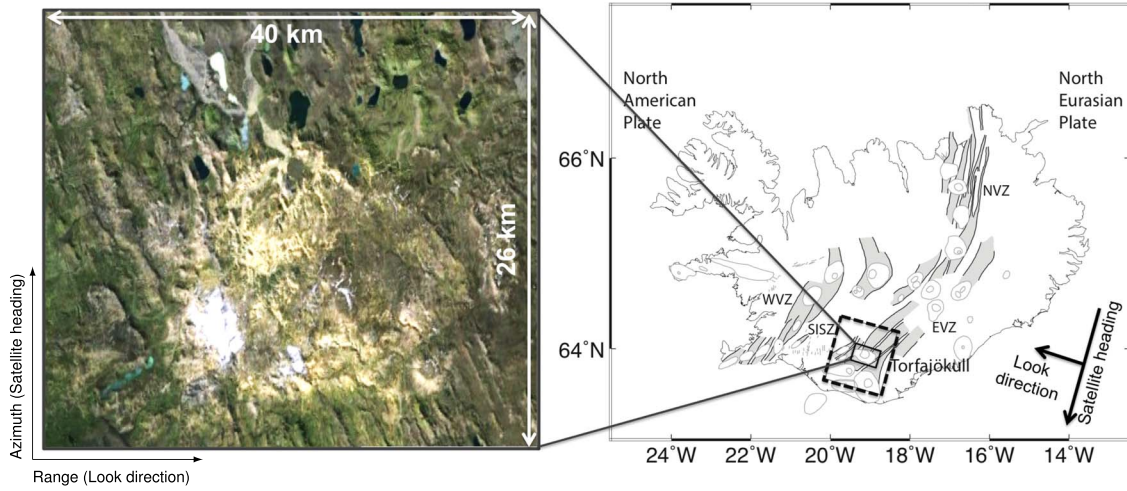
Fig. 13. (Right) Study area over Torfajökull volcano, Iceland. Torfajökull is located at the Eastern Volcanic Flank Zone (EVFZ). The black dashed rectangle is the location of the Envisat SAR scenes, while the black solid rectangle is the 40 × 26 km crop used in this study. (Left) Google Map view of the 40 × 26 km area of interest in radar coordinate system.
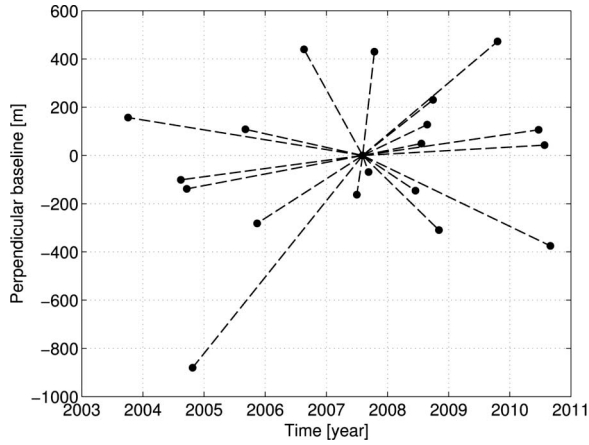

Fig. 14. Distribution of temporal and perpendicular baselines of the radar images used in the case study over Torfajökull volcano.

Fig. 15. Temporal coherence $\hat{\gamma}_{\mathrm{PTA}}$ for all pixels over the Torfajökull area. Higher values (≥ 0.7) indicate pixels with reliable SM-phase estimation. These pixels are selected as candidate coherent DS.

VII. CASE STUDY

We applied the ILS SM-phase estimation method to a stack of 20 Envisat SAR images (track 324), covering the period between September 03, 2003, and July 28, 2010, over Torfajökull volcano, Iceland (see Fig. 13). Torfajökull's latest eruption was in the 15th century, but the volcano caldera has been subsiding at linear rates in recent years [54]. We coregistered all slave images to an SM (July 04, 2007), which was chosen to minimize the average value of perpendicular and temporal baselines. The distribution of both temporal and perpendicular baselines of the radar images is depicted in Fig. 14. The crop used in the study is approximately 40 × 26 km wide (see Fig. 13).

The multilooked phases for each pixel are computed by spatial averaging over SHPs detected by Kolmogorov–Smirnov test, cf., [18]. The weight matrix was constructed based on estimated coherence values, using (27). In order to reduce the spatially variable signal within the multilooking areas, the topograph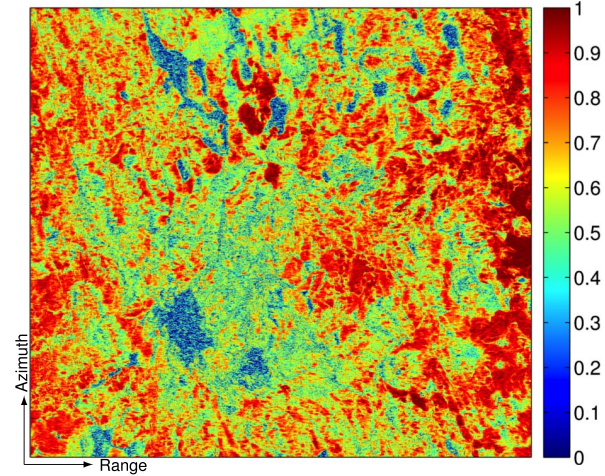ic phase component is computed and subtracted from all of the interferograms, using a 25-m digital elevation model from the national land survey of Iceland. We also apply the defringe algorithm presented in [43] during the multilooking step. After SHP selection and multilooking, we applied the ILS SM-phase estimation using all of the interferometric combinations. Then, for pixels with more than 50 SHP (in order to have a large number of looks), we replaced the phase of the original SM interferograms with the phase estimates of ILS SM-phase estimation. In order to evaluate where the SM-phase estimation is more effective, we plotted the $\hat{\gamma}_{\mathrm{PTA}}$ for all pixels in Fig. 15. The higher values (e.g., $\hat{\gamma}_{\mathrm{PTA}} \geq 0.7$) indicate pixels with reliably estimated SM-phases, hence candidates to be selected as coherent DSs. Fig. 16 shows four examples of *reconstructed* interferograms compared with the original single-looked interferograms. Visual investigation of these examples shows that SM-phase estimation can significantly improve the coherence by effectively filtering the noise components.
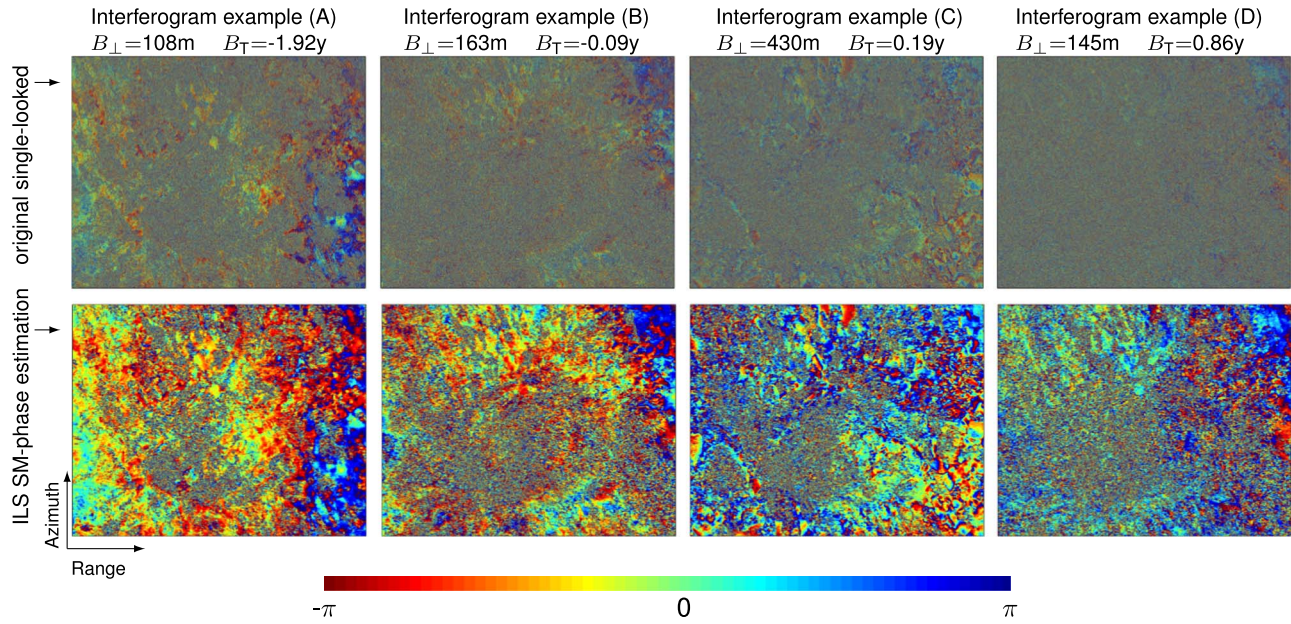
Fig. 16. Four examples of reconstructed interferograms by ILS SM-phase estimation (bottom row) compared with the original single-looked interferograms (top row). These examples show that the SM-phase estimation can significantly improve the coherence by effectively filtering the noise components.
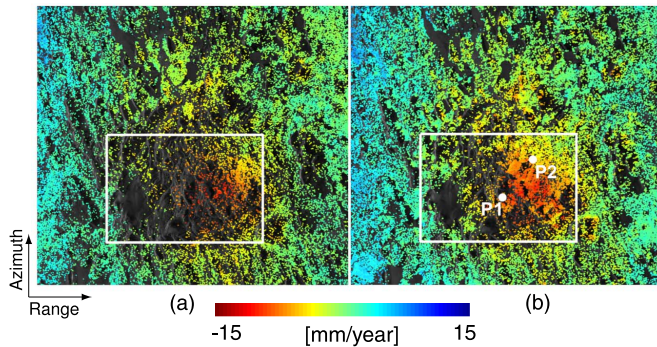

Fig. 17. Comparison between the velocity map applying StaMPS PS processing using (a) original single-look SM interferograms and (b) SM interferograms after ILS SM-phase estimation. The average velocity of the whole crop was used as a reference. The white rectangle shows the main subsiding area. The density of points improved from 32 000 to 72 000 (3300 to 13 000 in the deforming area). The deformation time-series of points P1 and P2 are plotted in Fig. 18(a) and (b).

In order to evaluate the added value of SM-phase estimation, we compare the results with the results with standard PSI processing when no SM-phase estimation is applied. For PSI processing, the StaMPS software was used [55], [56]. Both methods estimate a deformation of ∼10 cm in seven years. Within the volcano caldera, the surface is subsiding with a rate of ∼15 mm/year (attributed to a possible crystallization of a magma reservoir [54]). In order to have fair comparison, the same processing setup and selection criteria were used for both methods, except that, for the processing with SM-phase estimation, we also used an additional selection criterion, i.e., $\hat{\gamma}_{PTA} \geq 0.7$, on pixels with a number of SHP larger than 50. The final results are shown in Fig. 17, where the LOS velocity maps are plotted. These velocities are relative with respect to the average velocity of the whole crop. Using the standard method with single-looked interferograms, ∼32 000 coherent pixels were

identified in contrast with ∼72 000 identified coherent pixels via ILS SM-phase estimation. Over the main deforming area (the white rectangles in Fig. 17), the number of coherent pixels improved from 3300 to 13 000. Improvements in point density increase redundancy, leading to better precision, enhance the quality of the phase unwrapping and atmospheric removal, and allow the detection of spatially high-frequency deformation signal. Moreover, a higher density in the deforming areas can introduce more constraints in geophysical interpretation and subsurface modeling.

One of the main advantages of the ILS method is that it provides the precision or the full covariance matrix (i.e., $Q_{\hat{b}}$) of the inverted interferometric phases via (20). These matrices can be used as a proper weight matrix in further postprocessing or geophysical modeling of time-series InSAR results. Fig. 18(a) and (b) demonstrates two deformation time-series associated with the two pixels P1 and P2 identified with white dots in Fig. 17(b). The coherence matrix and the full covariance matrix of the inverted phases of these two pixels are visualized in Fig. 18(c)–(f), respectively. We should note that the $Q_{\hat{b}}$ in (20) is a function of the baseline configuration used in the estimation (via B matrix), the weight matrix (W), and the covariance matrix of multilooked interferometric phase (Q_y); the latter itself is a function of the target coherence matrix (C) and the number of looks (L). The difference in the covariance matrix of the inverted phases for pixels P1 and P2 is due to the different coherence matrices and different number of looks, which are 113 and 76 for P1 and P2, respectively. The higher the number of looks is, the smaller the variances are. The variable coherence structures and number of looks among detected DS result in deformation time-series with variable quality in time and space. Consequently, with DS, we are dealing with a set of deformation estimates with highly variable precision in time and apace. This important fact should be considered in further interpretation of the DS results.

(a) P1 deformation time-series

(b) P2 deformation time-series

(c) P1 coherence C_{P1}

(d) P2 coherence C_{P2}

(e) P1 covariance $Q_{\check{b}_{P1}}$

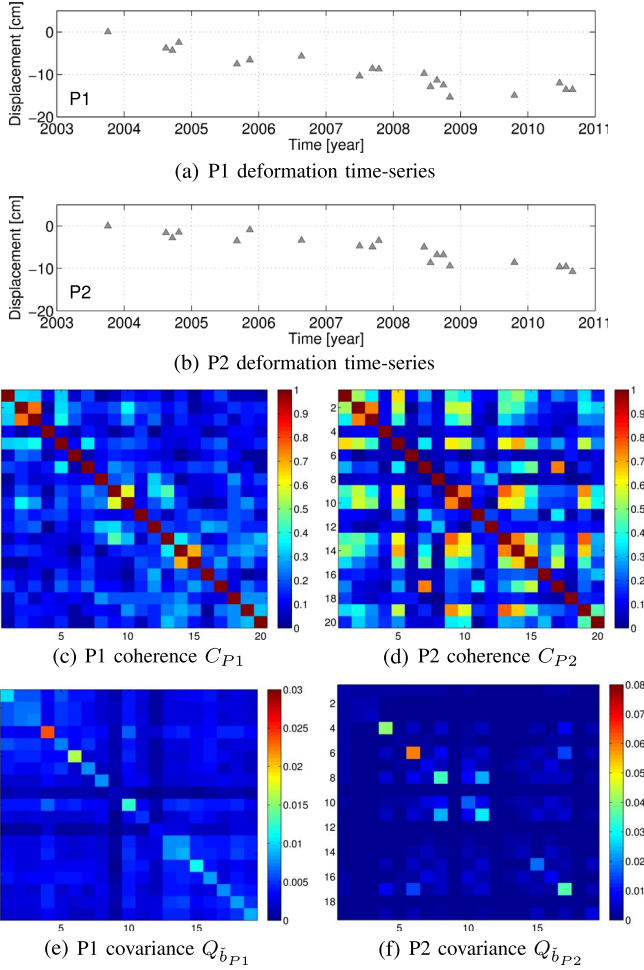(f) P2 covariance $Q_{\check{b}_{P2}}$

Fig. 18. Two example deformation time-series associated with (a) point P1 and (b) point P2 identified with white dots in Fig. 17(b). The coherence matrices of these two pixels are visualized in (c) and (d), and their full covariance matrices are visualized in (e) and (f), respectively. The phase covariances in (e) and (f) have been converted to square centimeters. The master image for construction of covariance matrices in (e) and (f) is the master image indicated in Fig. 14. (a) P1 deformation time-series. (b) P2 deformation time-series. (c) P1 coherence C_{P1}. (d) P2 coherence C_{P2}. (e) P1 covariance $Q_{\check{b}_{P1}}$. (f) P2 covariance $Q_{\check{b}_{P2}}$.

VIII. CONCLUSION

We have proposed a new method for estimating the SM interferometric phases from MM interferogram stacks, based on the ILS principle. The main advantages of ILS SM-phase estimation are the flexibility to be applied on any subset of interferograms and the quality description via the provision of a full covariance matrix of the estimates. The obtained covariance matrices can be further propagated to other InSAR derived parameters and can play an important role in the further postprocessing or geophysical modeling of time-series InSAR products. Via a simulation study, we have shown that the ILS SM-phase estimator is unbiased, and the closeness of the variance of its residuals with the lower CRB demonstrates the efficiency of the proposed approach. We have also demonstrated and discussed the influence of different factors such as detrending, weighting, and coherence bias on the efficiency of the ILS method. We have proposed a weighting strategy based on the

Fisher information index of multilooked interferometric phases and have demonstrated its efficiency. We have also compared the efficiency of the ILS with alternative estimators. The results show comparable or higher precision and efficiency for ILS compared to other estimators. The main drawback of the ILS approach is its high computational time, which needs to be improved. The proposed method has been successfully applied to a stack of interferograms over Torfajökull volcano in Iceland, resulting in double the number of detected coherent pixels with respect to conventional PSI.

APPENDIX A
IB ESTIMATOR

IB is an estimator to solve integer minimization problems with the form of

$$\check{a} = \underset{a \in \mathbb{Z}}{\arg\min} \|\hat{a} - a\|^2_{W_a} \qquad (30)$$

where

$$\hat{a} = [\hat{a}_1 \hat{a}_2 \ldots \hat{a}_n]^T. \qquad (31)$$

If W_a is a diagonal matrix, the solution of this minimization can simply be computed by rounding the entries of $\hat{a}$ to their nearest integer. However, in case of a full W_a, the nearest integer should be searched considering the mutual correlation among entries of $\hat{a}$, represented by off-diagonal elements in W_a. In order to do so, the IB estimator uses the concept of sequential conditional rounding, and the solution is computed as follows. First, the first entry $\hat{a}_1$ is rounded to its nearest integer. After that, all other elements of $\hat{a}$ are corrected based on their correlation with the first entry. Then, the second corrected entry is rounded to its nearest integer, etc. This sequence of corrections and roundings can be written mathematically as [57]

$$\check{b}_B = \begin{bmatrix} \check{b}_{B,1} \\ \check{b}_{B,2} \\ \vdots \\ \check{b}_{B,n} \end{bmatrix} = \begin{bmatrix} \text{nint}(\hat{a}_1) \\ \text{nint}\left(\hat{a}_2 - l_{21}(\hat{a}_1 - \check{b}_{B,1})\right) \\ \vdots \\ \text{nint}\left(\hat{a}_n - \sum_{i=1}^{n-1} l_{ni}\left(\hat{a}_{i|I} - \check{b}_{B,i}\right)\right) \end{bmatrix} \qquad (32)$$

where $\text{nint}(\cdot)$ is the nearest-integer rounding operator. The notation $\hat{a}_{i|I}$ stands for the ith real-valued entry obtained through a conditioning on the previous $I = 1, \ldots, i-1$ sequentially rounded entries. The elements l_{ji} are entries of a unit lower triangular matrix L computed from an LDL^T-decomposition of $W_a = LDL^T$.

APPENDIX B
CONSTRUCTION OF COHERENCE MATRICES

For the construction of the coherence values, four decorrelation sources were assumed.

1) *Thermal or system decorrelation*: the influence of thermal noise on system coherence depends on the signal-to-noise

(SNR) as [58]

$$\gamma_{\text{thermal}} = \frac{1}{1 + \text{SNR}^{-1}}. \tag{33}$$

The value for SNR is dependent on system parameters and radar scene's radar cross section (SCR), the latter varying subject to terrain characteristics. In this paper, we have assumed the system parameters of the ERS satellite (as reported in [48] and [59]) and an SCR of -14 dB, resulting in an SNR of 12 dB and a γ_{thermal} of 0.92.

2) *Coregistration-induced decorrelation*: this is mainly a function of the accuracy of image coregistration. Assuming subpixel coregistration accuracies of $\sigma_{\text{coreg},a}$ and $\sigma_{\text{coreg},r}$ in azimuth and range directions, the decorrelation induced by coregistration γ_{coreg} is computed as [33], [48]

$$\gamma_{\text{coreg}} = \text{sinc}(\sigma_{\text{coreg},a})\text{sinc}(\sigma_{\text{coreg},r}). \tag{34}$$

For the noise simulation here, we have assumed a coregistration accuracy of 0.1 resolution cell in both azimuth and range directions, resulting in $\gamma_{\text{coreg}} = 0.96$.

3) *Geometric decorrelation*: The geometric or baseline decorrelation is a result of different incidence angles between the two radar paths at the Earth's surface. For an interferometric pair of two radar images, geometric decorrelation is defined as [48]

$$\gamma_{\text{geom}} = \max\left(1 - \frac{|B_\perp|}{B_{\perp_{\max}}}, 0\right) \tag{35}$$

where $B_\perp$ is the perpendicular baseline between two images and $B_{\perp_{\max}}$ is the critical baseline. In this simulation, the critical baseline is assumed as 1.1 km, which is equal to the ERS critical baseline for flat terrains. Perpendicular baselines are simulated randomly as normally distributed with zero mean and standard deviation of 300 m.

4) *Temporal decorrelation*: As the range of physical mechanisms causing temporal decorrelation is too wide, there is no single analytical model to evaluate coherence loss induced by this effect. In this paper, we have assumed two arbitrary scenarios for temporal decorrelation: exponential decay and seasonal decay. In case of exponential decay, the temporal coherences are modeled as [60]

$$\gamma_{\text{temp}} = e^{\frac{B_T}{\tau}} \tag{36}$$

where B_T is the temporal baseline and τ is the *decorrelation rate*, assumed here to be 200 days. For the seasonal-effect scenario, it is assumed that the coherence is exponentially decreasing but has also some seasonal variation. This is realistic for areas with some degree of coherence during winter but very low coherence during summer or vice versa. Such behavior has been observed by [61] in pasture areas.

After computing all of the aforementioned coherences, the total simulated coherence (γ_{sim}) is derived as

$$\gamma_{\text{sim}} = \gamma_{\text{thermal}}\gamma_{\text{coreg}}\gamma_{\text{geom}}\gamma_{\text{temp}}. \tag{37}$$

By computing the γ_{sim} for all of the interferometric combinations and for the two temporal decorrelation scenarios, we construct the two coherence matrices C_e and C_s for the exponential-decay and seasonal-decay scenarios, respectively, visualized in Fig. 2.

REFERENCES

[1] A. Ferretti, C. Prati, and F. Rocca, "Nonlinear subsidence rate estimation using permanent scatterers in differential SAR interferometry," *IEEE Trans. Geosci. Remote Sens.*, vol. 38, no. 5, pp. 2202–2212, Sep. 2000.

[2] A. Ferretti, C. Prati, and F. Rocca, "Permanent scatterers in SAR interferometry," *IEEE Trans. Geosci. Remote Sens.*, vol. 39, no. 1, pp. 8–20, Jan. 2001.

[3] B. Kampes and R. Hanssen, "Ambiguity resolution for permanent scatterer interferometry," *IEEE Trans. Geosci. Remote Sens.*, vol. 42, no. 11, pp. 2446–2453, Nov. 2004, doi: 10.1109/TGRS.2004.835222

[4] B. M. Kampes and N. Adam, "The STUN algorithm for persistent scatterer interferometry," in *Proc. 4th Int. Workshop ERS/Envisat SAR Interferometry, FRINGE*, Frascati, Italy, Nov. 28–Dec. 2, 2005, pp. 1–14. [Online]. Available: http://adsabs.harvard.edu/full/2006ESASP.610E..16K

[5] A. Hooper, H. Zebker, P. Segall, and B. Kampes, "A new method for measuring deformation on volcanoes and other non-urban areas using InSAR persistent scatterers," *Geophys. Res. Lett.*, vol. 31, no. 23, Dec. 2004, Art. no. L23611, doi: 10.1029/2004GL021737.

[6] F. van Leijen, "Persistent Scatterer Interferometry Based on Geodetic Estimation Theory," Ph.D. dissertation, Dept. Geosci. Remote Sens., Delft Univ. Technol., Delft, The Netherlands, Apr. 2014.

[7] H. A. Zebker, P. A. Rosen, and S. Hensley, "Atmospheric effects in interferometric synthetic aperture radar surface deformation and topographic maps," *J. Geophys. Res.*, vol. 102, no. B4, pp. 7547–7563, Apr. 1997.

[8] T. Wright, B. Parsons, and E. Fielding, "Measurement of interseismic strain accumulation across the North Anatolian Fault by satellite radar interferometry," *Geophys. Res. Lett.*, vol. 28, no. 10, pp. 2117–2120, May 2001.

[9] T. J. Wright, B. Parsons, P. C. England, and E. J. Fielding, "InSAR observations of low slip rates on the major faults of western Tibet," *Science*, vol. 305, pp. 236–239, Jul. 9, 2004.

[10] D. T. Sandwell and E. J. Price, "Phase gradient approach to stacking interferograms," *J. Geophys. Res.*, vol. 103, no. B12, pp. 30 183–30 204, Dec. 1998.

[11] S. Usai, "A New Approach for Long Term Monitoring of Deformations by Differential SAR Interferometry," Ph.D. dissertation, Delft Inst. for Earth-Oriented Space Res., Delft Univ. Technol., Delft, The Netherlands, 2001.

[12] S. Usai, "A least squares database approach for SAR interferometric data," *IEEE Trans. Geosci. Remote Sens.*, vol. 41, no. 4, pp. 753–760, Apr. 2003, doi: 10.1109/TGRS.2003.810675.

[13] O. Mora, J. J. Mallorqui, and A. Broquetas, "Linear and nonlinear terrain deformation maps from a reduced set of interferometric SAR images," *IEEE Trans. Geosci. Remote Sens.*, vol. 41, no. 10, pp. 2243–2253, Oct. 2003.

[14] D. A. Schmidt and R. Bürgmann, "Time-dependent land uplift and subsidence in the Santa Clara Valley, California, from a large interferometric synthetic aperture radar data set," *J. Geophys. Res.*, vol. 108, no. B9, pp. 2416–2428, Sep. 2003, doi: 10.1109/TGRS.2003.810675.

[15] P. Berardino, G. Fornaro, R. Lanari, and E. Sansosti, "A new algorithm for surface deformation monitoring based on small baseline differential SAR interferograms," *IEEE Trans. Geosci. Remote Sens.*, vol. 40, no. 11, pp. 2375–2383, Nov. 2002.

[16] R. Lanari, O. Mora, M. Manunta, J. J. Mallorquï, P. Berardino, and U. Sansosti, "A small-baseline approach for investigating deformations on full-resolution differential SAR interferograms," *IEEE Trans. Geosci. Remote Sens.*, vol. 42, no. 7, pp. 1377–1386, Jul. 2004.

[17] A. Monti-Guarnieri and S. Tebaldini, "On the exploitation of target statistics for SAR interferometry applications," *IEEE Trans. Geosci. Remote Sens.*, vol. 46, no. 11, pp. 3436–3443, Nov. 2008.

[18] A. Ferretti, A. Fumagalli, F. Novali, C. Prati, F. Rocca, and A. Rucci, "A new algorithm for processing interferometric data-stacks: SqueeSAR," *IEEE Trans. Geosci. Remote Sens.*, vol. 49, no. 9, pp. 3460–3470, Sep. 2011.

[19] A. Pepe, Y. Yang, M. Manzo, and R. Lanari, "Improved EMCF-SBAS processing chain based on advanced techniques for the noise-filtering and selection of small baseline multi-look DInSAR interferograms," *IEEE Trans. Geosci. Remote Sens.*, vol. 53, no. 8, pp. 4394–4417, Aug. 2015.

[20] G. Fornaro, S. Verde, D. Reale, and A. Pauciullo, "CAESAR: An approach based on covariance matrix decomposition to improve multibaseline–multitemporal interferometric SAR processing," *IEEE Trans. Geosci. Remote Sens.*, vol. 53, no. 4, pp. 2050–2065, Apr. 2015.

[21] N. Cao, H. Lee, and H. Jung, "A phase-decomposition-based PSInSAR processing method," *IEEE Trans. Geosci. Remote Sens.*, vol. 54, no. 2, pp. 1074–1090, Feb. 2016.

[22] B. Pinel-Puysségur, R. Michel, and J. Avouac, "Multi-link InSAR time series: Enhancement of a wrapped interferometric database," *IEEE J. Sel. Topics Appl. Earth Observ. Remote Sens.*, vol. 5, no. 3, pp. 784–794, Jun. 2012.

[23] S. Samiei-Esfahany and R. F. Hanssen, "New algorithm for InSAR stack phase triangulation using integer least squares estimation," in *Proc. Int. Geosci. Remote Sens. Symp.*, Melbourne, Vic., Australia, Jul. 21–26, 2013, pp. 884–887.

[24] P. J. G. Teunissen, "Least-squares estimation of the integer GPS ambiguities," in *Proc. Invited Lecture, Section IV Theory Methodol., IAG Gen. Meet.*, Beijing, China, Aug. 1993, pp. 1–16, also in: Delft Geodetic Computing Centre, LGR Series, No. 6, 1994.

[25] P. J. G. Teunissen, "The least-squares ambiguity decorrelation adjustment: A method for fast GPS integer ambiguity estimation," *J. Geodesy*, vol. 70, no. 1/2, pp. 65–82, 1995.

[26] P. J. G. Teunissen and A. Kleusberg, Eds., *GPS for Geodesy*, 2nd ed. Berlin, Germany: Springer-Verlag, 1998.

[27] R. F. Hanssen and A. Ferretti, "Parameter estimation in PS-InSAR deformation studies using integer least-squares techniques," *EOS Trans. AGU, Fall Meet. Suppl., Abstract G62A-06*, vol. 83, no. 47, p. F37, 2002.

[28] R. F. Hanssen, P. J. G. Teunissen, and P. Joosten, "Phase ambiguity resolution for stacked radar interferometric data," in *Proc. Int. Symp. Kinematic Syst. Geodesy, Geomatics Navigat.*, Banff, AB, Canada, Jun. 5–8, 2001, pp. 317–320. [Online]. Available: http://plan.geomatics.ucalgary.ca/papers/PDF/0602.PDF

[29] P. J. G. Teunissen, "On InSAR ambiguity resolution for deformation monitoring," *Artif. Satell.*, vol. 41, no. 1, pp. 17–22, 2006. [Online]. Available: http://www.degruyter.com/view/j/arsa.2006.41.issue-1/v10018-007-0002-8/v10018-007-0002-8.xml

[30] S. N. Madsen, "Speckle Theory: Modelling, Analysis, and Applications Related to Synthetic Aperture Radar Data," Ph.D. dissertation, Dept. of Electromagn. Syst., Tech. Univ. Denmark, Lyngby, Denmark, 1986.

[31] R. Bamler and P. Hartl, "Synthetic aperture radar interferometry," *Inv. Probl.*, vol. 14, pp. R1–R54, 1998. [Online]. Available: http://geo.uzh.ch/microsite/rsl-documents/research/SARlab/GMTILiterature/Ver09/PDF/BH98b.pdf

[32] J. S. Lee, K. W. Hoppel, S. A. Mango, and A. R. Miller, "Intensity and phase statistics of multilook polarimetric and interferometric SAR imagery," *IEEE Trans. Geosci. Remote Sens.*, vol. 30, no. 5, pp. 1017–1028, Sep. 1994.

[33] D. Just and R. Bamler, "Phase statistics of interferograms with applications to synthetic aperture radar," *Appl. Opt.*, vol. 33, no. 20, pp. 4361–4368, 1994.

[34] R. J. A. Tough, D. Blacknell, and S. Quegan, "A statistical description of polarimetric and interferometric synthetic aperture radar," *Proc. R. Soc. London A*, vol. 449, no. 4, pp. 567–589, 1995.

[35] K. Sarabandi, "Derivation of phase statistics from the Mueller matrix," *Radio Sci.*, vol. 27, no. 5, pp. 553–560, Sep./Oct. 1992.

[36] M. Lucido, F. Meglio, V. P. Pascazio, and G. Schirinzi, "Closed-form evaluation of the second-order statistical distribution of the interferometric phases in dual-baseline SAR systems," *IEEE Trans. Geosci. Remote Sens.*, vol. 58, no. 3, pp. 1698–1707, Mar. 2010.

[37] B. Gundlich, K. Koch, and J. Kusche, "Gibbs sampler for computing and propagating large covariance matrices," *J. Geodesy*, vol. 77, no. 9, pp. 514–528, Dec. 2003.

[38] J. Rice, *Mathematical Statistics and Data Analysis*, 3rd ed. Pacific Grove, CA, USA: Duxbury Press, Apr. 2001.

[39] M. S. Seymour and I. G. Cumming, "Maximum likelihood estimation for SAR interferometry," in *Proc. Int. Geosci. Remote Sens. Symp.*, Pasadena, CA, USA, Aug. 8–12, 1994, pp. 2272–2275.

[40] A. Parizzi and R. Brcic, "Adaptive InSAR stack multilooking exploiting amplitude statistics: A comparison between different techniques and practical results," *IEEE Geosci. Remote Sens. Lett.*, vol. 8, no. 3, pp. 441–445, May 2011.

[41] Y. Wang, X. X. Zhu, and R. Bamler, "Retrieval of phase history parameters from distributed scatterers in urban areas using very high resolution SAR data," *ISPRS J. Photogramm. Remote Sens.*, vol. 73, pp. 89–99, 2012.

[42] K. Goel and N. Adam, "A distributed scatterer interferometry approach for precision monitoring of known surface deformation phenomena," *IEEE Trans. Geosci. Remote Sens.*, vol. 52, no. 9, pp. 5454–5468, Sep. 2014.

[43] M. Jiang, X. Ding, and Z. Li, "Hybrid approach for unbiased coherence estimation for multitemporal InSAR," *IEEE Trans. Geosci. Remote Sens.*, vol. 52, no. 5, pp. 2459–2473, May 2014.

[44] M. Jiang, X. Ding, R. Hanssen, R. Malhotra, and L. Chang, "Fast statistically homogeneous pixel selection for covariance matrix estimation for multitemporal InSAR," *IEEE Trans. Geosci. Remote Sens.*, vol. 53, no. 3, pp. 1213–1224, Mar. 2015.

[45] Y. Wang and X. X. Zhu, "Robust estimators for multipass SAR interferometry," *IEEE Trans. Geosci. Remote Sens.*, vol. 54, no. 2, pp. 968–980, Feb. 2016.

[46] G. W. Davidson and R. Bamler, "Multiresolution phase unwrapping for SAR interferometry," *IEEE Trans. Geosci. Remote Sens.*, vol. 37, no. 1, pp. 163–174, Jan. 1999.

[47] H. A. Zebker and K. Chen, "Accurate estimation of correlation in InSAR observations," *IEEE Geosci. Remote Sens. Lett.*, vol. 2, no. 2, pp. 1682–1690, Apr. 2005.

[48] R. Hanssen, *Radar Interferometry: Data Interpretation and Error Analysis*. Dordrecht, The Netherlands: Kluwer, 2001.

[49] I. R. Joughin and D. P. Winebrenner, "Effective number of looks for a multilook interferometric phase distribution," in *Proc. Int. Geosci. Remote Sens. Symp.*, Pasadena, CA, USA, Aug. 8–12, 1994, pp. 2276–2278.

[50] R. Touzi, A. Lopes, and P. W. Vachon, "Estimation of the coherence function for interferometric SAR applications," in *Proc. Eur. Conf. Synthetic Aperture Radar*, Königswinter, Germany, Mar. 26–28, 1996, pp. 241–244.

[51] R. Touzi, A. Lopes, J. Bruniquel, and P. W. Vachon, "Coherence estimation for SAR imagery," *IEEE Trans. Geosci. Remote Sens.*, vol. 37, no. 1, pp. 135–149, Jan. 1999.

[52] F. De Zan, M. Zonno, and P. Lopez Dekker, "Phase inconsistencies and multiple scattering in SAR interferometry," *IEEE Trans. Geosci. Remote Sens.*, vol. 53, no. 12, pp. 6608–6616, Dec. 2015.

[53] S. Jazaeri, A. R. Amiri-Simkooei, and M. A. Sharifi, "Fast integer least-squares estimation for GNSS high-dimensional ambiguity resolution using lattice theory," *J. Geodesy*, vol. 86, no. 2, pp. 123–136, Feb. 2011.

[54] S. E. Scheiber-Enslin, P. C. LaFemina, E. Sturkell, A. J. Hooper, and S. J. Webb, "Geodetic investigation of plate spreading along a propagating ridge: The Eastern Volcanic Zone, Iceland," *Geophys. J. Int.*, vol. 187, no. 3, pp. 1175–1194, Dec. 2011.

[55] A. Hooper, "Persistent Scatterer Radar Interferometry for Crustal Deformation Studies and Modeling of Volcanic Deformation," Ph.D. dissertation, Dept. Geophys., Stanford Univ., Stanford, CA, USA, 2006.

[56] A. Hooper, D. Bekaert, K. Spaans, and M. Arkan, "Recent advances in SAR interferometry time series analysis for measuring crustal deformation," *Tectonophysics*, vol. 514, pp. 1–13, 2012.

[57] P. J. G. Teunissen, "Success probability of integer GPS ambiguity rounding and bootstrapping," *J. Geodesy*, vol. 72, pp. 606–612, 1998.

[58] H. A. Zebker and J. Villasenor, "Decorrelation in interferometric radar echoes," *IEEE Trans. Geosci. Remote Sens.*, vol. 30, no. 5, pp. 950–959, Sep. 1992.

[59] H. A. Zebker, P. A. Rosen, R. M. Goldstein, A. Gabriel, and C. L. Werner, "On the derivation of coseismic displacement fields using differential radar interferometry: The Landers earthquake," *J. Geophys. Res.*, vol. 99, no. B10, pp. 19 617–19 634, Oct. 10, 1994.

[60] F. Rocca, "Modeling interferogram stacks," *IEEE Trans. Geosci. Remote Sens.*, vol. 45, no. 10, pp. 3289–3299, Oct. 2007.

[61] Y. Morishita and R. F. Hanssen, "Temporal decorrelation in L-, C-, and X-band satellite radar interferometry for pasture on drained peat soils," *IEEE Trans. Geosci. Remote Sens.*, vol. 53, no. 2, pp. 1096–1104, Feb. 2015.

Sami Samiei-Esfahany received the B.Sc. degree in civil-surveying engineering from Amirkabir University of Technology, Tehran, Iran, in 2004 and the M.Sc. degree in geomatics engineering from the Delft University of Technology (TU Delft), Delft, The Netherlands, in 2007.

In 2008, he joined TU Delft as a Ph.D. student, working on InSAR research. His studies regard new algorithms in time-series InSAR processing and optimal estimation of surface displacement induced by gas extraction/injection using satellite radar interferometry, with main focus on stochastic aspects of observations. Since 2013, he has been a Researcher with the Department of Geoscience and Remote Sensing, TU Delft. His current research interests include estimation theory and mathematical geodesy with applications to SAR interferometry and deformation monitoring.

Joana Esteves Martins graduated as Geodesy Engineer from the Faculty of Sciences, University of Lisbon, Lisbon, Portugal, in 2006 and received the Master's degree in geophysics from the University of Lisbon, Lisbon, Portugal, in 2008, with a research project focusing on the deformation using radar interferometry of Faial and Pico volcanic islands in the Azores archipelago. She has been working toward the Ph.D. degree in the Department of Geoscience and Remote Sensing, Delft University of Technology, Delft, The Netherlands, since 2010. Her Ph.D. topic concerns understanding volcanic plumbing systems using radar and seismic interferometry, with main focus on Icelandic volcanoes.

Freek van Leijen received the Master's degree in geodetic engineering from the Delft University of Technology, Delft, The Netherlands, in 2002. His thesis concerned the stochastic modeling of the tropospheric variability using GPS and InSAR observations.

In 2003, he rejoined the Delft University of Technology as a Ph.D. student, working on InSAR research. He has developed a range of software algorithms for persistent scatterer interferometry. After working five years at SkyGeo, a commercial company delivering radar remote sensing services, he returned to the Delft University of Technology in 2013 to continue his research in the field of satellite radar interferometry.

Ramon F. Hanssen (M'04) received the M.Sc. degree in geodetic engineering and the Ph.D. (*cum laude*) degree from the Delft University of Technology, Delft, The Netherlands, in 1993 and 2001, respectively.

He was with the International Institute for Aerospace Survey and Earth Science (ITC), Stuttgart University, Stuttgart, Germany; the German Aerospace Center (DLR); Stanford University, Stanford, CA, USA (Fulbright Fellow); and the Scripps Institution of Oceanography in microwave remote sensing, radar interferometry, signal processing, and geophysical application development. Since 2008, he has been an Antoni van Leeuwenhoek Professor in earth observation with Delft University of Technology, where he has been leading the research group on mathematical geodesy and positioning since 2009. He is the author of a textbook on radar interferometry.